

Rupture dynamics and ground motion from 3-D rough-fault simulations

Zheqiang Shi,¹ and Steven M. Day¹

Received 5 October 2012; revised 14 January 2013; accepted 15 January 2013.

[1] We perform three-dimensional (3-D) numerical calculations of dynamic rupture along non-planar faults to study the effects of fault roughness on rupture propagation and resultant ground motion. The fault roughness model follows a self-similar fractal distribution over length scales spanning three orders of magnitude, from $\sim 10^2$ to $\sim 10^5$ m. The fault is governed by a strongly rate-weakening friction, and the bulk material is subject to Drucker-Prager viscoplasticity. Fault roughness promotes the development of self-healing rupture pulses and a heterogeneous distribution of fault slip at the free surface and at depth. The inelastic deformation, generated by the large dynamic stress near rupture fronts, occurs in a narrow volume around the fault with heterogeneous thickness correlated to local roughness slopes. Inelastic deformation near the free surface, however, is induced by the stress waves originated from dynamic rupture at depth and spreads to large distances (>10 km) away from the fault. The present simulations model seismic wave excitation up to ~ 10 Hz with rupture lengths of ~ 100 km, permitting comparisons with empirical studies of ground-motion intensity measures of engineering interest. Characteristics of site-averaged synthetic response spectra, including the distance and period dependence of the median values, absolute level, and intra-event standard deviation, are comparable to appropriate empirical estimates throughout the period range 0.1–3.0 s. This class of model may provide a viable representation of the ground-motion excitation process over a wide frequency range in a large spatial domain, with potential applications to the numerical prediction of source- and path-specific effects on earthquake ground motion.

Citation: Shi, Z., and S. M. Day (2013), Rupture dynamics and ground motion from 3-D rough-fault simulations, *J. Geophys. Res. Solid Earth*, 118, doi:10.1002/jgrb.50094.

1. Introduction

[2] Natural faults during their evolutionary stages manifest varying degrees of geometrical complexities over a broad range of scales spanning from larger-scale features such as branching and segmentation [e.g., *Ben-Zion and Sammis*, 2003; *Bryant*, 2005] to smaller-scale features such as topographic variations on the fault slip surfaces [e.g., *Power and Tullis*, 1991; *Renard et al.*, 2006; *Sagy et al.*, 2007; *Sagy and Brodsky*, 2009; *Candela et al.*, 2009, 2012; *Bistacchi et al.*, 2011]. Microscopically, surface roughness can influence the frictional properties by affecting the distribution and evolution of contact areas of the sliding surface. Moreover, the geometric irregularities of the fault can induce local variations of the stress distribution around the fault both during and between seismic events. The aforementioned roles of fault roughness can have a significant impact on earthquake

processes, including nucleation, propagation, and termination [e.g., *Chester and Chester*, 2000; *Campillo et al.*, 2001; *Dieterich and Smith*, 2009; *Griffith et al.*, 2010].

[3] Previous theoretical studies indicated that earthquake rupture propagation along a rough-fault surface could excite high-frequency radiation as rupture fronts accelerate, decelerate, or lose coherence from the interaction with geometric irregularities [e.g., *Madariaga*, 1977; *Boore and Joyner*, 1978; *Kame and Uchida*, 2008]. Meanwhile, changes of rupture properties such as the amplitude and shape of the slip rate induced by fault roughness can lead to a heterogeneous distribution of fault slip. Using 2-D plane-strain model simulations, *Dunham et al.* [2011b] studied the effects of self-similar fault roughness on dynamic rupture propagation. A heterogeneous slip distribution was observed, along with fluctuations of rupture front speed that led to the excitation of high-frequency accelerations having characteristics resembling observational data.

[4] In the present work, we perform 3-D simulations of dynamic ruptures on a rough fault with a vertical mean plane, using SORD [*Ely et al.*, 2008, 2009, 2010], with additional implementation of new constitutive relations for the fault interface and the bulk material. This study is an initial exploration in 3-D of the influence of fault roughness on the spontaneous rupture propagation and resultant ground motion. Our large-scale simulations that account for the

¹Department of Geological Sciences, San Diego State University, San Diego, CA 92182-1020, USA.

Corresponding author: Z. Shi, Department of Geological Sciences, San Diego State University, San Diego, CA 92182-1020, USA. (zshi@projects.sdsu.edu)

©2013. American Geophysical Union. All Rights Reserved. 2169-9313/13/10.1002/jgrb.50094

lithostatic stress distribution, free-surface interactions, and 3-D wave propagation effects should provide useful insights into the role of fault roughness in natural seismic events. To isolate effects of fault-surface roughness in this initial study, we neglect the heterogeneities in initial shear and normal stresses (apart from smooth depth dependence) in the surrounding volume that will inevitably accompany the fault roughness.

[5] Motivated by recent high-speed rock sliding experiments [e.g., *Tsutsumi and Shimamoto*, 1997; *Di Toro et al.*, 2004; *Han et al.*, 2010; *Goldsby and Tullis*, 2011], we employ a rate- and state-dependent (RSD) friction with a strongly rate-weakening feature to characterize the fault frictional behavior. We adopt Drucker-Prager viscoplasticity [*Drucker and Prager*, 1952], allowing off-fault plastic strain to relax what would otherwise be unphysically high stress concentrations in the dynamic process around the rupture tip [*Andrews*, 2005; *Ben-Zion and Shi*, 2005; *Templeton and Rice*, 2008] and the roughness slopes [*Duan and Day*, 2008; *Dunham et al.*, 2011b].

[6] The model of fault roughness used in our simulations is self-similar over a limited range of scales (roughly from 10^2 to 10^5 m) with its power spectrum following a power law characterized by Hurst exponent H equal to 1. The self-similar model represents a simplification, in that both anisotropy and departure from self-similarity have been noted in recent observational studies of fault morphology. For example, *Renard et al.* [2006], *Sagy et al.* [2007], and *Candela et al.* [2009] suggested self-affine fault roughness with some degrees of anisotropy. However, their high-resolution data showing anisotropy are limited to scales less than ~ 100 m, which is about the shortest wavelength present in our roughness model. Furthermore, *Bistacchi et al.* [2011], based on observations on low-slip faults, suggest that anisotropy is limited principally to scales less than or comparable to the total slip. Thus, we consider it appropriate not to include anisotropy in fault roughness distribution for the current study.

[7] As pointed out by *Dunham et al.* [2011b], characterizing data from a wide range of scales using a single power law is problematic. For example, *Candela et al.* [2012] noted that data sets obtained at disparate scales (ranging from 10^{-4} to 10^5 m) individually appear to be self-affine with Hurst exponents in the range between 0.6 and 0.8. However, due to the variation of the power law prefactors across (and within) different scales, a power law with $H=1$ actually connects the large (map scale) and intermediate (outcrop scale) data sets in their compilation better than any single power law curve with $H=0.8$ [see *Candela et al.*, 2012, Figure 13]. We therefore consider the conceptually simpler self-similar model of 2-D fault roughness justified and appropriate for parameterizing the present model calculations.

[8] In section 2, we describe our model setup and outline the solution methods. In section 3, we provide detailed analyses of results from our 3-D simulations of a rough-fault rupture model, with emphasis on rupture properties, surface slip, patterns of associated plastic deformation, and characteristics of resultant ground motion. We defer more detailed sensitivity studies, recognizing that a comprehensive model of rupture and ground motion will eventually require integrating both surface roughness and heterogeneity of initial stress field in a self-consistent manner. Nonetheless, we are able to show that

even in its present simplified form, the rough-fault model successfully parameterizes a substantial range of important statistical features of recorded ground motions.

2. Problem Formulation and Solution Methods

[9] We first describe the generation of surface roughness of the fault used in our simulations (details given in Appendix A) along with the 3-D model geometry, followed by the constitutive relations employed for the fault (details given in Appendix B) and for the bulk material, respectively. We then describe the hypothesized initial stress state and the method of artificial rupture nucleation. Finally, the numerical solution methods employed are outlined.

2.1. Self-Similar Fault Surface and Model Geometry

[10] We generated 2-D self-similar fault roughness using a Fourier transform method [*Andrews and Barall*, 2011] described in Appendix A. The self-similar property of the synthetic 2-D fault surface holds for a limited wavelength range $[\lambda_{\min}, \lambda_{\max}]$. The maximum roughness wavelength λ_{\max} is set to be the horizontal extent of the modeled fault. Changes of fault roughness characteristics are controlled by two other parameters: the short-wavelength cutoff λ_{\min} and the amplitude-to-wavelength ratio α (see definition in Appendix A). Estimates of α for natural faults typically lie in the range 10^{-3} – 10^{-2} [e.g., *Power and Tullis*, 1991].

[11] Figure 1 shows the synthetic fault roughness pattern, model geometry, and coordinate system used in our 3-D simulations. The self-similar fault roughness is generated with $\lambda_{\min}=80$ m and $\alpha=10^{-2.3} \approx 0.005$. The mean plane of the rough fault located at $x_3=0$ is at 90° to the flat free surface (at $x_2=0$). The fault system is subjected to a right-lateral strike-slip sense of loading. In a 2-D strike-slip system with fault irregularities, we have restraining bends, where stress loading leads to a local increase of normal compression, and releasing bends, where stress loading leads to a local reduction of normal compression (Figure 2). Similarly, in a 3-D strike-slip rough-fault system, we can define restraining and releasing slopes in analogy to the restraining and releasing bends in 2-D, respectively.

2.2. Fault Constitutive Relation

[12] The fault constitutive relation is characterized by an RSD friction with a strongly rate-weakening feature combined with a regularized normal traction response (see Appendix B). The definitions of the friction parameters and their values used in our simulations are all specified in Table 1. As shown in Figure 3, friction parameters a and V_w are set to be depth dependent such that the fault frictional behavior transitions from velocity weakening in the middle seismogenic section to velocity strengthening in both the upper section near the free surface and the lower section beneath the seismogenic zone (values of a and V_w in Table 1 are for the middle seismogenic section). The lower velocity-strengthening transition confines nearly all slip to depths shallower than ~ 16 km. In order to prevent further rupture propagation beyond the model domain, narrow transition zones of friction from velocity weakening to velocity strengthening are added near the outer boundaries with normals parallel to the x_1 -axis, effectively confining rupture to a fault segment of ~ 80 km long. Figure 3 also shows the magnitudes of depth-dependent initial shear

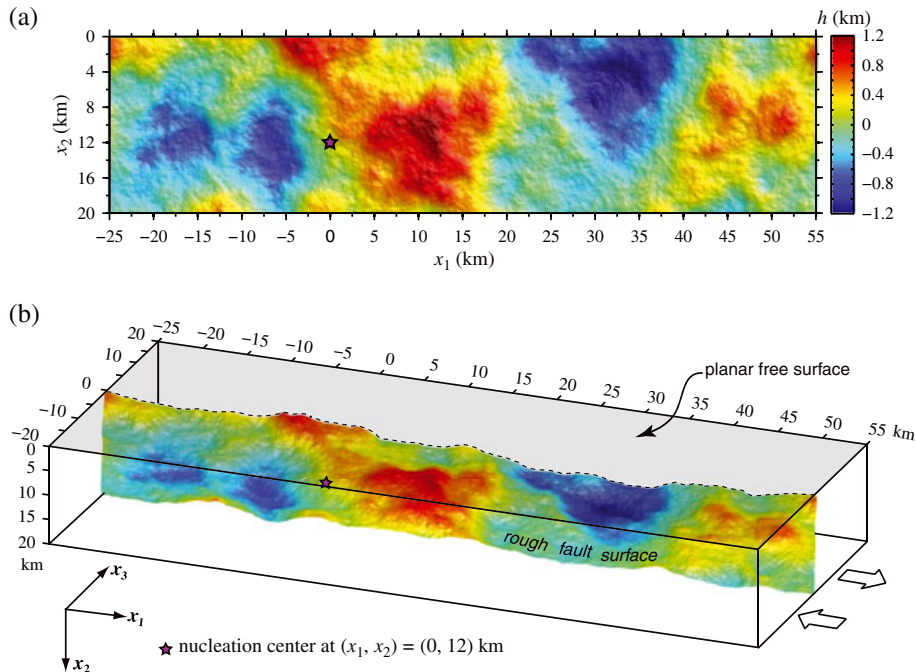


Figure 1. (a) Synthetic self-similar fault roughness generated with $\lambda_{\min} = 80$ m and $\alpha = 10^{-2.3}$ (viewed from the $-x_3$ side of the fault). The color scale denotes deviation of the rough-fault surface from the vertical mean plane. (b) Model geometry, dimensions, and coordinate system for 3-D numerical simulations. The initial shear stresses are applied in right-lateral strike-slip sense of motion. Rupture nucleation center is located at $(x_1, x_2) = (0, 12)$ km.

and effective normal stresses (see section 2.4) resolved onto the vertical mean plane of the rough fault.

[13] To ensure numerical convergence, the cohesive zone where the evolution of friction state at the rupture front occurs has to be resolved sufficiently well by the numerical grid. Approximating the evolution of fault strength at the rupture front under the RSD friction with equivalent slip-weakening parameters [e.g., *Shi et al.*, 2008; *Dunham et al.*, 2011a], we estimate the size of the cohesive zone Λ (for rupture on a planar fault) using the formula given by *Palmer and Rice* [1973] for the dominant rupture mode in our simulation (mode II). With the employed friction parameters (Table 1), the estimated cohesive zone size as a function of depth in the velocity-weakening fault section ($a < b$) is shown in the right-most panel of Figure 3. Rough estimates of Λ obtained by examining shear traction profiles at various depths and time steps from simulations showed good agreement with the theoretical values. Even at the bottom of the velocity-weakening section where Λ is at its minimum of 112 m, the cohesive zone is still adequately resolved with our 20 m grid spacing used in this study. For instance, at this level of resolution, the benchmark solution metrics for rupture time, slip, and shear traction examined by *Day et al.* [2005] and *Rojas et al.* [2009] all showed relative errors below 1%, and those for slip velocity showed relative errors of $\sim 10\%$ or less.

2.3. Off-Fault Elastoplasticity Model

[14] The Drucker-Prager plasticity model [*Drucker and Prager*, 1952], which has been widely used in geomechanics to describe the pressure-dependent inelastic yielding of materials such as rocks and concretes, is a generalization of the Huber-von Mises yield criterion with the addition of

hydrostatic stress dependence of the yield surface. The Drucker-Prager yield criterion employed here is given by

$$\begin{aligned} \bar{\tau} &\leq \tau^v \\ \bar{\tau} &= \sqrt{\frac{1}{2}s_{ij}s_{ij}} \\ \tau^v &= -\frac{1}{3}\sigma_{kk}\sin\phi + c\cos\phi \end{aligned} \quad (1)$$

where $s_{ij} = \sigma_{ij} - \frac{1}{3}\sigma_{kk}\delta_{ij}$ are the deviatoric stress components, c is the cohesion, and ϕ is the angle of internal friction. Since pore fluid pressure is taken into account in prescribing the initial stress distribution, all of the stresses mentioned in this paper are effective stresses unless otherwise noted.

[15] The Drucker-Prager yield surface is a smooth approximation to the Mohr-Coulomb yield surface and plots as a cylindrical cone in the principal stress space (Figure 4). To inhibit extreme localization of plastic deformation, a Maxwellian viscoplasticity scheme [e.g., *Andrews*, 2005; *Duan and Day*, 2008; *Ma and Andrews*, 2010] is used for the adjustment of s_{ij} during plastic yielding to bring the

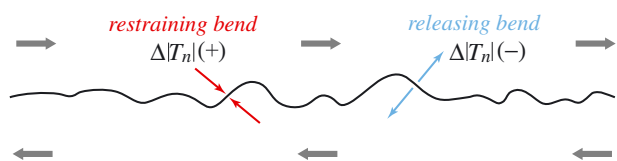


Figure 2. A schematic diagram illustrating the definitions of releasing and restraining bends in a 2-D strike-slip rough-fault model. Stress loading leads to the increase of normal compression at restraining bends and the reduction of normal compression at releasing bends.

Table 1. Model Parameter Values

Parameter		Value
<i>Bulk Properties</i>		
Shear wave speed	c_s	3464 m/s
Shear modulus	G	32.04 GPa
Poisson's ratio	ν	0.25
Cohesion	c	5 MPa
Internal friction coefficient	$\tan(\phi)$	0.75
<i>Frictional Properties</i>		
Direct-effect parameter	a	0.01
Evolution-effect parameter	b	0.014
Reference slip rate	V_0	1 $\mu\text{m/s}$
Steady-state coefficient at slip rate V_0	f_0	0.7
Evolution distance of state variable ψ	L	0.2 m
Weakening slip rate	V_w	0.1 m/s
Fully weakened friction coefficient	f_w	0.2
Evolution distance of traction variable θ_{PC}	L_{PC}	0.2 m
Initial fault slip rate	V^{mi}	6×10^{-11} m/s
<i>Fault Roughness Properties</i>		
Amplitude-to-wavelength ratio	α	$10^{-2.3}$
Minimum wavelength	λ_{min}	80 m

stress state smoothly toward the yield surface over time. Zero volumetric plastic strain is assumed, and the accumulated (shear) plastic strain magnitude η is defined as

$$\eta = \int \sqrt{\frac{2}{3} d\epsilon_{ij}^p d\epsilon_{ij}^p} \quad (2)$$

where $d\epsilon_{ij}^p = ds_{ij}/(2\mu)$ is the (shear) plastic strain increment and ds_{ij} is the adjustment of deviatoric stress at one time step, respectively.

2.4. Initial Stress State and Rupture Nucleation

[16] The elastic and viscoplastic properties of the bulk material in the model are uniform. Assuming lithostatic stress loading and hydrostatic pore pressure, the effective initial normal stresses are given by $\sigma_{11}^0 = \sigma_{22}^0 = \sigma_{33}^0 = -(\rho - \rho_w)gx_2$, where g is the gravitational acceleration, and ρ and ρ_w are the densities of rock and water, respectively. A combination of initial shear stresses that produces a right-lateral strike-slip sense

of motion is assumed: $|\sigma_{31}^0| = |\sigma_{22}^0|/3$ and $\sigma_{12}^0 = \sigma_{23}^0 = 0$. With this prescribed initial stress state (Figure 3), the maximum compressive prestress is at 45° to the mean fault plane.

[17] For all simulation cases in this study, rupture nucleation is achieved by imposing at time $t=0$ a shear traction perturbation $\Delta\tau_0(x_1, x_2)$ on a finite fault patch centered at $(x_1^h, x_2^h) = (0, 12)$ km with radius $R=1$ km, i.e.,

$$\Delta\tau_0(x_1, x_2) = \exp\left(\frac{r^2}{r^2 - R^2}\right) H(R-r) \tau_0(x_1, x_2) \quad (3)$$

where H is the Heaviside step function, $r = \sqrt{(x_1 - x_1^h)^2 + (x_2 - x_2^h)^2}$, and $\tau_0(x_1, x_2)$ is the heterogeneous shear traction obtained by resolving the equilibrium initial stresses onto the rough fault.

2.5. Solution Methods

[18] We solve the equations described in Appendix B and section 2.3, together with 3-D viscoelastic equations of motion, using SORD [Ely *et al.*, 2008]. This code uses a generalized finite difference method; the spatial discretization follows a second-order accurate support operator scheme [e.g., Shashkov, 1996] on a structured hexahedral grid, and the time integration is explicit. After sampling the rough-fault surface at a $20 \text{ m} \times 20 \text{ m}$ grid spacing parallel to the x_1 - x_2 plane, we construct a mesh of ~ 9.45 billion cells that contains all of these fault-surface sample points within one of its logical coordinate planes while maintaining ~ 20 m intervals in each coordinate direction (Figure 5). The fault points are represented by split nodes using the method of Ely *et al.* [2009]. The RSD equations (B1)–(B7) are solved using the staggered velocity-state method of Rojas *et al.* [2009] that is further modified to accommodate the addition of state equation (B8). We added an elastoplastic solver to SORD, based on a trial-stress formulation [e.g., Simo and Hughes, 1998, p.15], with regularization via a time-dependent relaxation scheme [e.g., Andrews, 2005]. The full methodology, including an off-fault elastoplastic response, has been verified

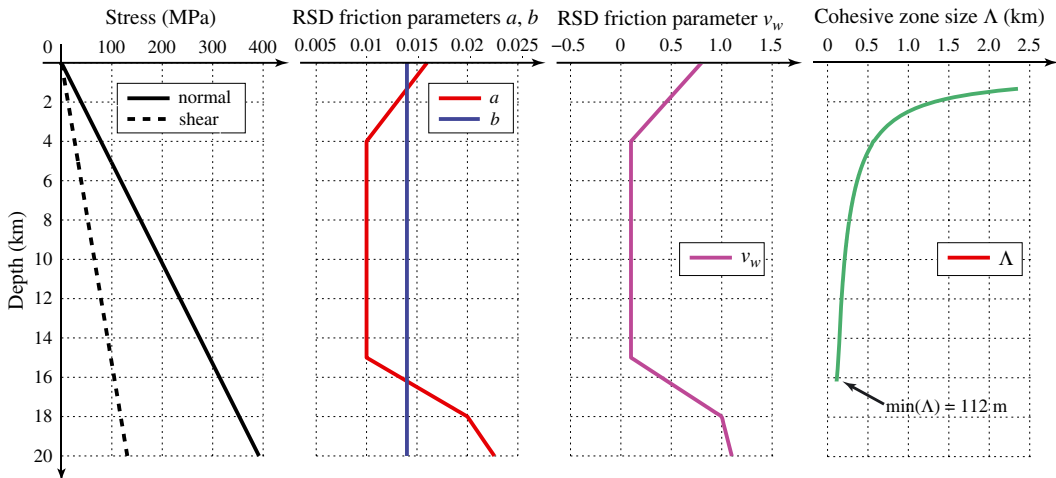


Figure 3. Magnitudes of initial normal and shear stresses resolved onto the mean fault plane, RSD friction parameters (a , b , and v_w), and theoretically estimated cohesive zone size Λ as functions of depth employed for numerical simulations. Estimation of cohesive zone size is only shown for the velocity-weakening section where $a < b$.

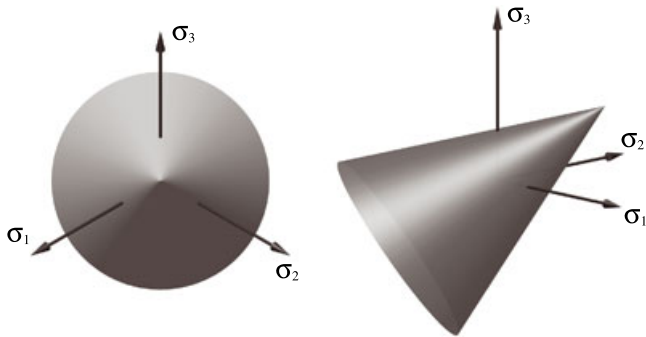


Figure 4. Yield surface of the Drucker-Prager yield criterion in 3-D space of principal stresses. The symmetry axis of the regularly shaped cone is along $\sigma_1 = \sigma_2 = \sigma_3$.

using test problems developed by the Southern California Earthquake Center [Harris *et al.*, 2009]. One simulation run of 20-sec dynamic rupture propagation takes ~ 6.25 hours using 16,384 processors on Kraken Cray XT5 at the Oak Ridge National Laboratory.

3. Numerical Results

[19] In this section, we present simulation results focusing on the effects of fault roughness on the spontaneous rupture process, the patterns of resultant plastic deformation, and ground motion.

3.1. Rupture Characteristics

[20] Figure 6 shows snapshots of slip rate along the rough fault at 2 s intervals. The relatively coherent initial slip patch originated from the nucleation zone quickly evolves into two major pulse-like slip patches propagating in opposite directions. The spontaneous rupture is largely concentrated in the middle velocity-weakening section of the fault. Low confining pressure at shallow depth allows for a small amount of shallow slip triggered by radiated stress waves from rupture fronts at depth. The releasing and restraining slopes have opposite effects on rupture propagation, as is well illustrated by slip-rate snapshots at times 10, 12, and 14 s. The top portion of the main rupture front initially dies gradually as it encounters a fault region dominated by restraining slopes from $t=10$ –12 s and then recovers along a region dominated by releasing slopes from $t=12$ –14 s. Contours of rupture times (defined in the figure caption) in Figure 7 suggest that the main rupture fronts remain relatively smooth for the most part and propagate at a relatively steady sub-Rayleigh speed (~ 3 km/s). In contrast, the healing fronts appear rather ragged, with fluctuating propagation speeds, suggesting a strong influence from the presence of fault roughness.

[21] The final distribution of normal traction change $\Delta|T_n|$ and shear traction change $\Delta|T_s|$ (Figure 8) exhibits a great amount of heterogeneity, the smallest wavelength of which is on the scale of λ_{\min} . In particular, close inspection reveals that there tends to be an overall magnitude increase of normal and shear tractions (positive $\Delta|T_n|$ and $\Delta|T_s|$) on slip regions dominated by restraining slopes. The pattern of final fault slip shows interesting correlation with the fault roughness (Figure 9). For instance, there is general

suppression of slip on fault regions dominated by restraining slopes, the extreme case being the nonslipping areas along the upper friction transition zone between $x_1=18$ km to $x_1=35$ km where rupture propagation is inhibited.

[22] The final surface slip along the fault trace also exhibits a considerable amount of heterogeneity (Figure 10), with a profile showing apparent anticorrelation with the local slopes of the fault-surface trace. Fluctuations of surface slip on the order of several tens of percent are present over length scales of a few hundred meters.

[23] The simulated rupture event has a moment magnitude $M_w=7.23$, and the time history of the seismic moment rate is shown in Figure 11. In a comparison simulation carried out with λ_{\min} doubled, i.e., from 80 to 160 m, and other model parameters unchanged, the dynamic rupture exhibits similar characteristics but appears slightly more coherent. As a result, the seismic moment rate follows a similar trend but has larger overall amplitudes, leading to an increase of moment magnitude M_w from 7.23 to 7.33. These effects of varying λ_{\min} reflect the fact that resistance to slip is dominated by the shortest roughness wavelengths. As shown by Dunham *et al.* [2011b], under the assumption of linear elasticity, the root-mean-square (rms) normal stress perturbation induced by slip Δu scales as $\alpha\Delta u/\lambda_{\min}$. Nonetheless, inelastic processes will undoubtedly limit the growth of these perturbations at the shortest length scales [e.g., Dieterich and Smith, 2009].

[24] To better illustrate effects of fault roughness on the rupture process, we show in Figure 12 snapshots of the slip rate and traction changes $\Delta|T_n|$ and $\Delta|T_s|$ at time $t=4$ s from a comparison simulation with a planar fault and all other model parameters unchanged. Comparing Figure 12 with Figure 6, we can see that the self-healing rupture pulse is much better developed in the rough-fault case. Changes of normal traction $\Delta|T_n|$ in the planar-fault case are present only near the rupture fronts due to plastic yielding, whereas in the rough-fault case, there are multitudinous fluctuations in the slipped regions behind the rupture fronts (Figure 8). Similar contrasts between planar and rough cases are also found in the shear traction change $\Delta|T_s|$, which in the rough-fault case

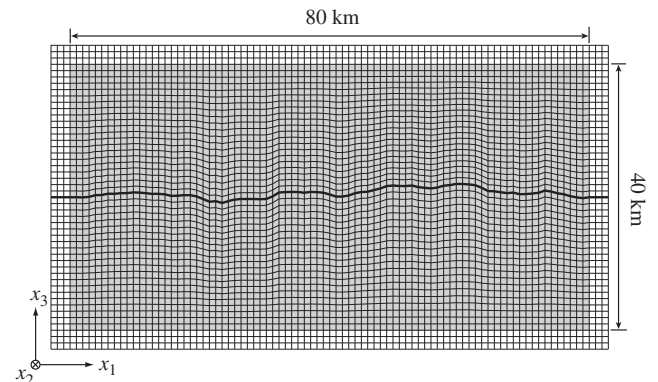


Figure 5. Map view of a horizontal cross section of the mesh, schematically shown in low resolution for illustration purposes. Regularly spaced cells for the PML zone are added near the outer boundaries. The thick curve represents the fault line where this mesh cross-section intersects the rough-fault plane at a certain depth. Grid lines within the gray area are linearly interpolated in the x_3 direction.

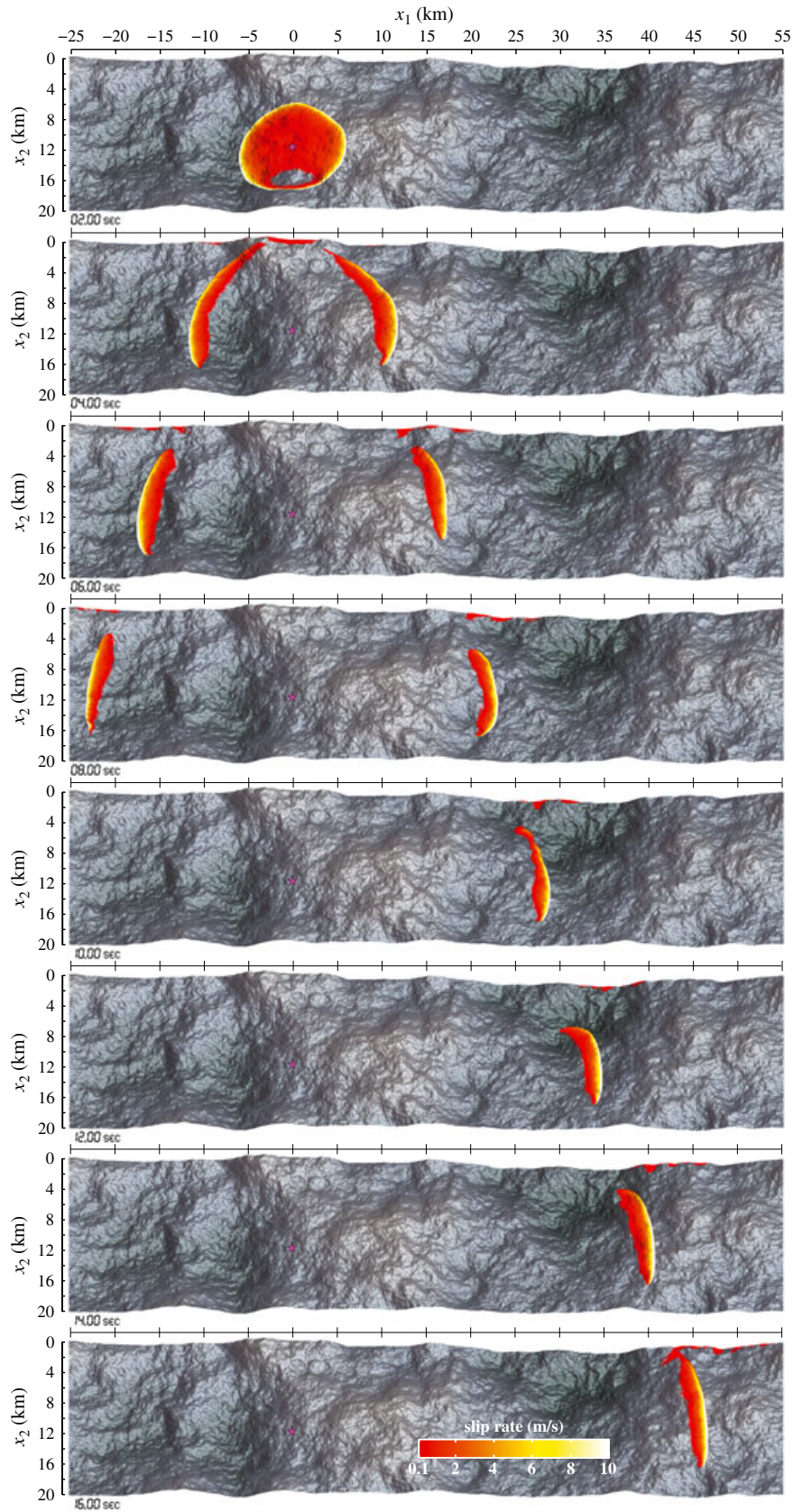


Figure 6. Snapshots of slip rate along the rough fault at 2 s intervals from time $t = 2$ s to $t = 16$ s. The view angle is parallel to the $+x_3$ direction.

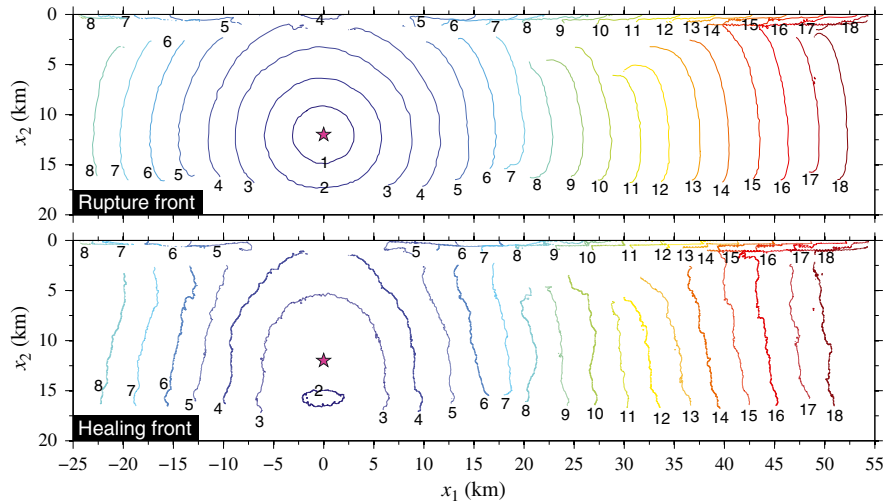


Figure 7. Contours of rupture and healing fronts at 1 s intervals mapped onto the x_1 - x_2 plane. The hypocenter location is indicated as a star symbol. The threshold value of slip rate for the determination of rupture and healing fronts is 0.1 m/s.

shows overall reduction in the slipped regions with a significant amount of fluctuations.

3.2. Plastic Strain Distribution

[25] Figure 13 shows the distribution of accumulated plastic strain η at 10 m depth (the center of the topmost layer of model cells). At this depth, plastic yielding is mainly triggered by stress waves radiated from the large dynamic stress changes near rupture fronts at depth. According to equation (1), the cohesion parameter c plays a much larger role in limiting plastic yielding at shallow depths than it does at greater depths, where the cohesion term in the yield stress becomes negligible compared with the pressure-dependent term. With lower cohesion, we would expect near-surface plastic deformation to be even more extensive and of larger magnitude. As shown in the inset in Figure 13, there is distinct absence of plastic deformation in areas of immediate proximity to the fault trace in this simulation. This absence is most likely due to the presence of the top velocity-strengthening layer (depth ~ 1.67 km) (Figure 3), which imposes a shadowing effect on

the generation of strong motion and occurrence of plastic yielding. This example illustrates the degree to which near-surface friction and prestress conditions can affect predictions of near-fault behavior. Future work will need to consider more realistic models for these near-surface conditions and their evolution over multiple earthquake occurrences.

[26] At distances much further away from the fault, the near-surface inelastic response is less sensitive to the shallow frictional behavior of faulting. The degree of inelastic straining as a function of fault-normal distance (measured from the mean fault plane) is summarized in Figure 14 (at 10 m depth as in Figure 13). The model predicts substantial irreversible strain induced by ground motion persisting to fault-normal distances of up to 5–10 km. The spatial extent is larger than that obtained by *Ma and Andrews* [2010] with a crack-like rupture on a planar fault, for the same cohesion value of 5 MPa. This difference is simply due to the much longer rupture propagation in our model simulation, which is shown in Figure 13, where the extent of inelastic straining in the fault-normal direction grows as the rupture extends. For the same

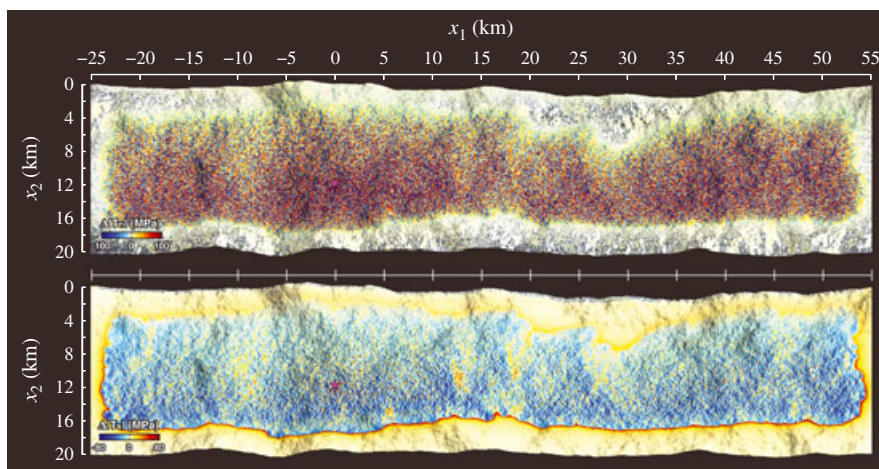


Figure 8. Final distribution of (top) normal traction change $\Delta|T_n|$ and (bottom) shear traction change $\Delta|T_s|$ from their respective initial levels (at $t=0$) along the rough fault.

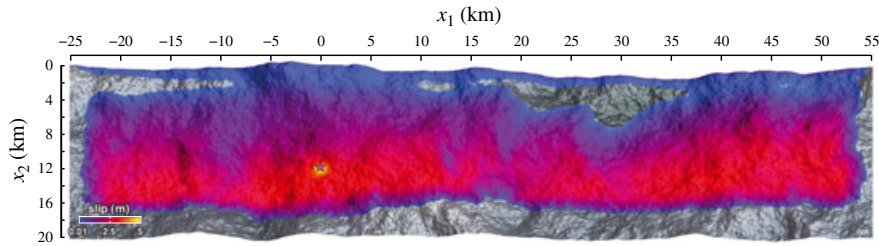


Figure 9. Final distribution of fault slip. The variations of slip amplitude correlate with the distribution of releasing and restraining slopes.

rupture propagation distance and comparable stress condition, however, typically less inelastic straining is expected from pulse-like ruptures (as in the current simulation) than from crack-like ruptures, due to the difference in the magnitude of associated dynamic stress changes [e.g., *Ben-Zion and Shi, 2005; Shi et al., 2010; Xu et al., 2012*].

[27] The time histories of deviatoric stress components (s_{ij}), yield stress ($\bar{\tau}$, τ^p), and accumulated plastic strain (η) at Locations 1–4 (indicated in Figure 13) are shown in Figure 15. At Locations 1 and 2, which are relatively closer to the fault, the initial occurrence of plastic yielding happens before the arrival of the hypocentral S wave. In contrast, at Locations 3 and 4, which are further away, the initial plastic yielding happens slightly after the arrival of the hypocentral S wave. Common to all near-surface locations, nevertheless, is that the majority of the plastic yielding is induced by seismic energy arriving after the hypocentral S phase.

[28] Figure 16 shows cross-section views of the along-depth distribution of accumulated plastic strain η at various along-strike distances. Plastic deformation along deeper portions of the fault is generated by large local stress changes at rupture fronts. The general pattern of plastic deformation being widespread in the very shallow part of the model but quickly narrowing down to a small volume surrounding the fault at depth (mostly on the extensional side) is qualitatively similar to the results by *Ma and Andrews [2010]*, but the details differ substantially, mainly due to the model differences in fault geometry (rough versus planar) and rupture mode (pulse-like versus crack-like). Absence of accumulated plastic strain is observed around fault sections where rupture propagation is inhibited due to the presence of (1) a velocity-weakening-to-strengthening transition zone at relatively shallow depth (<4 km) and (2) restraining slopes, as shown in Figure 16f. Except for the fault areas close to the nucleation

center, plastic strain at depth is mostly concentrated on the extensional side of the fault with a relatively stable width that is moderately modulated by local roughness slopes. A close-up view of the accumulated plastic strain at hypocentral depth $x_2 = 12$ km shown in Figure 17 reveals properties similar to those shown in Figure 16, as do sections at other depths in most of the velocity-weakening fault region.

3.3. Ground Motion

[29] The rupture irregularities lead to ground motions of considerable complexity, as previously shown in the 2-D simulations of *Dunham et al. [2011b]*. Figure 18 shows snapshots of the fault-parallel acceleration and velocity fields at the free surface at time $t = 8$ s. The ground acceleration shows extensive high-frequency content from many rupture fronts originated from spontaneous rupture irregularities along deeper portions of the rough fault. Formed behind the hypocentral S wavefront are distinctive cone-shaped patterns associated with small surface slip that is induced in the velocity-strengthening zone and propagates at high apparent horizontal velocity between $x_1 = 20$ km and $x_1 = 25$ km. In comparison, the velocity field is much smoother, as would be expected, especially given our omission of heterogeneity in the initial stress field. The distortion of the radiation pattern due to fault roughness is well illustrated by the striking departure of the P -wave nodal surface (the polarity boundary ahead of the hypocentral S wavefront) from the fault surface trace.

[30] The three-component accelerograms at surface stations at $x_1 = 9$ km labeled in the top plot of Figure 18 are shown in Figure 19. These stations are all within 9 km of the mean fault plane. Even in the absence of scattering in the medium (recall that the simulations are performed with a uniform half-space), accelerations exceeding 0.1 g persist for at least 10 s or more in most records.

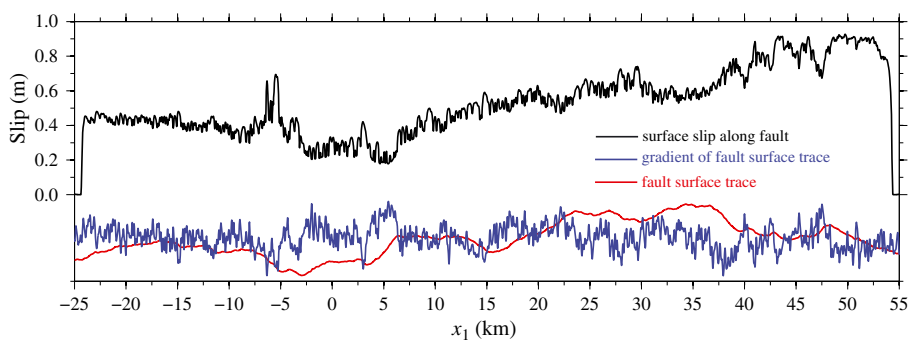


Figure 10. Profile of final slip along the surface fault trace aligned with the profiles of fault surface trace and its gradient.

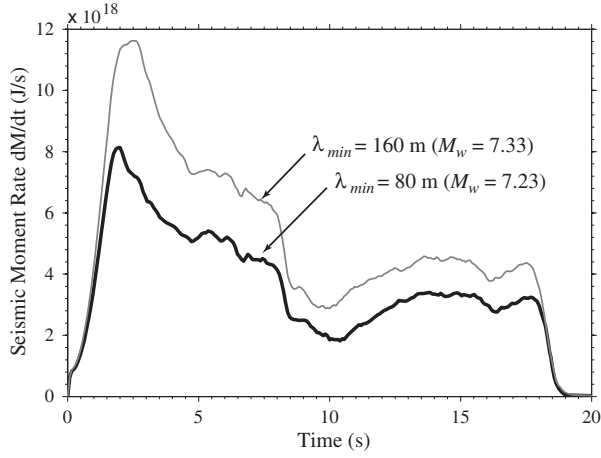


Figure 11. Time histories of seismic moment rate from spontaneous rupture propagation on rough faults with $\lambda_{\min} = 80$ m and $\lambda_{\min} = 160$ m, respectively.

[31] Fourier spectra of the acceleration records, such as those shown in Figure 20a, indicate that the acceleration spectra are roughly flat between a few tenths of a hertz and an upper cutoff frequency of slightly less than 10 Hz. Fourier spectra of recorded ground motion exhibit a similar upper cutoff frequency, conventionally called f_{\max} [Hanks, 1982], and we adopt that term here, although without suggesting that the simulated f_{\max} has the same physical significance as empirical f_{\max} (as our model neglects path effects such as viscoelastic losses that probably dominate most empirical f_{\max} estimates). The f_{\max} value of the simulation records does not noticeably vary across the surface stations, and its dependence on model parameters can be seen most clearly in the average normalized Fourier spectra, as shown in Figure 20b, where we compare the spectral averages from simulations with and without off-fault plasticity (the elastic

case is constrained to disallow fault opening). The comparison in Figure 20b shows that the energy dissipation in the medium due to inelastic deformation results in a pronounced downward shift of f_{\max} relative to the calculation without plasticity, with a concomitant decrease of high-frequency spectral amplitude. A very similar downward shift of f_{\max} occurs when the minimum roughness wavelength λ_{\min} is doubled, and an upward shift of similar magnitude occurs when the state evolution slip L of the RSD friction is halved.

[32] Contours of the fault-parallel, fault-normal, vertical, and geometric-mean peak ground acceleration (PGA) are shown in Figure 21. Patterns of considerable spatial variability overlay the overall decay of PGA with fault-normal distance. The level of this variability appears to be quantitatively similar to that found in earthquake strong motion records (in a sense that is discussed in section 4), despite the lateral uniformity of the initial stress state in the volume and of frictional properties on the fault. The off-fault plastic yielding that contributed to the lowering of the f_{\max} in ground acceleration also plays a significant role in the overall PGA magnitude: the PGA measurements from the corresponding simulation without plasticity are, on average, $\sim 50\%$ larger than those from the simulation with plasticity shown in Figure 21.

[33] The geometric mean of an intensity measure (e.g., PGA or a response spectral ordinate) for a fixed pair of recorded horizontal components of motion is not very well suited for quantifying ground-motion intensity, due to its dependence on the orientation of the recording instruments. Therefore, recent empirical ground-motion prediction equations (GMPEs) have adopted orientation-independent averages of the component intensity measures, e.g., the so-called GMRotD50 and GMRotI50 values [Boore *et al.*, 2006]. GMRotD50, for instance, is the median of the geometric-mean values of the response spectra for two orthogonal horizontal motion components rotated through a set of equally spaced angles between 0° and 90° .

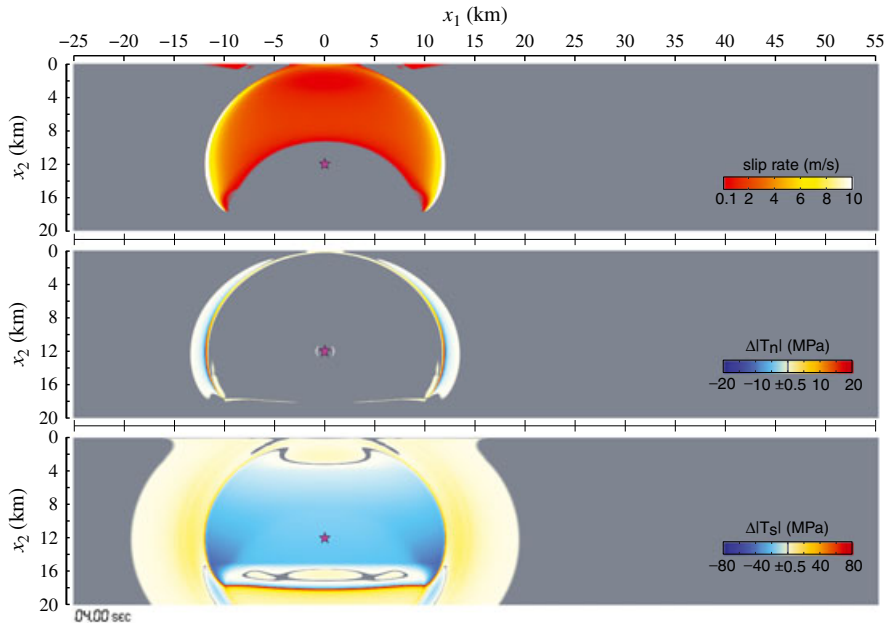


Figure 12. Snapshots of slip rate, changes of normal traction $\Delta|T_n|$, and shear traction $\Delta|T_s|$ from their respective initial levels at time $t = 4$ s in the comparison simulation with a planar fault.

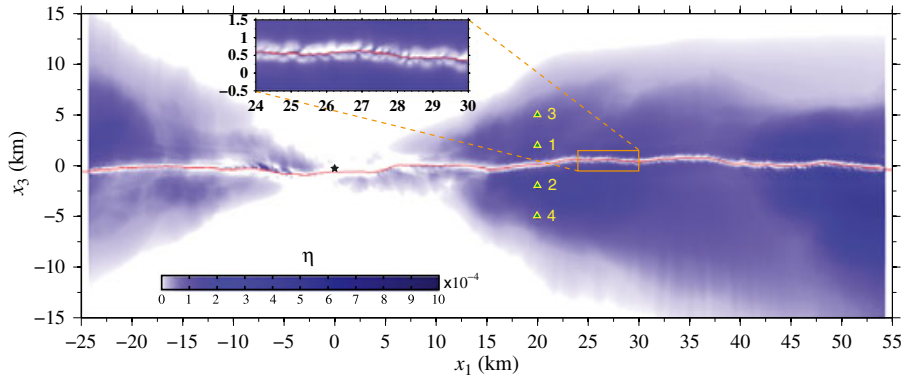


Figure 13. Distribution of accumulated plastic strain η at 10 m depth (center of the topmost computational cell layer). The inset shows a close-up view of η in a portion of the immediate vicinity of the fault. The epicenter location is indicated by a star symbol. The time histories of various stresses and cumulative plastic strain η at locations labeled 1–4 are shown in Figure 15.

[34] We compute GMRotD50 response spectra for representative periods from 0.1 to 3.0 s for comparison with four of the GMPEs developed for the Next Generation Attenuation (NGA) project [Power *et al.*, 2008]. The more complicated GMRotI50 was used for the GMPE development, but simulation averages for GMRotD50 and GMRotI50 are essentially indistinguishable. We will use four GMPEs that employ a similar set of predictor variables: the NGA equations of Abrahamson and Silva [2008] (denoted by AS), Campbell and Bozorgnia [2008] (CB), Boore and Atkinson [2008] (BA), and Chiou and Youngs [2008] (CY). This set of GMPEs is a useful benchmark against which to compare averages of intensity measures extracted from a suite of simulations. Moreover, as we have previously found, because of the large number of synthetic ground-motion sites available for averaging, even a single simulation can begin to yield informative comparisons [e.g., Olsen *et al.*, 2008, 2009]. Such comparisons can be used to evaluate the capability of a model to capture those ensemble measures of ground motion (such as a median spectral ordinate and its dependence upon period and distance) that are relatively well constrained by existing observations. Some acceptable level of consistency with the ensemble properties of existing strong motion records is probably a minimum requirement for a simulation method to serve as a credible predictive tool for earthquake ground motion; once such consistency is established, numerical simulations will provide a means to account for additional source-, path- and site-specific information that is not represented in the current empirical GMPEs. Furthermore, this kind of comparison is especially useful when assessing models for high-frequency excitation, since the approach averages out essentially unpredictable stochastic effects in the source and the path. The range of the median estimates from the above set of GMPEs spans much, although not all, of the epistemic uncertainty in the median, making it useful to retain all four in our comparison.

[35] The rock site recordings that constrain the GMPEs [Chiou *et al.*, 2008] are almost entirely from sites with near-surface S velocity (V_{s30}) lower than about 1200 m/s and with attenuation parameter κ averaging around 0.03–0.04 s [e.g., Boore and Joyner, 1997; Campbell, 2003]. Here κ is the site anelastic loss exponent defined by Anderson and Hough

[1984] such that the Fourier spectrum at frequency f is attenuated by factor $e^{-\pi\kappa f}$. Except for an artificial viscosity term that is effective only at very high frequencies, the simulations were performed using a half-space without anelastic attenuation. To obtain a meaningful comparison, we correct our simulation time histories by filtering them with the SH plane-wave response of the generic rock structure designed by Boore and Joyner [1997] to be representative of the western North America rock sites that are predominant in the strong motion database. The site attenuation is also included in this filtering process, with attenuation parameter $\kappa = 0.04$ s.

[36] The red curves in Figure 22 are the geometric-mean response spectral acceleration values computed from the site-corrected simulation time histories. Each point on the curve corresponds to a GMRotD50 spectral acceleration averaged (averaging on the natural logarithm) across all the stations with the same Joyner-Boore distance R_{jb} , which in this case is the same as the fault-normal distance, in the range [1, 15] km. We will refer to them as the simulation

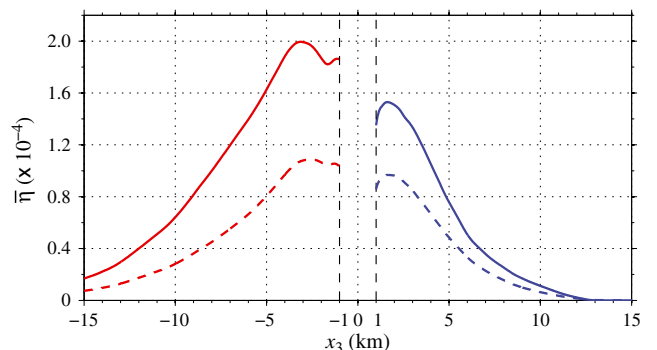


Figure 14. Plastic strain $\bar{\eta}$ averaged over the plastic deformation field shown in Figure 13 along the x_1 direction as a function of x_3 , the fault-normal distance measured from the mean fault plane. Due to the wavy nature of the fault trace, zones of $x_3 = [-1, 1]$ km are excluded from the averaging operation. The solid and dashed curves correspond to values from averaging over along-strike (x_1) distance intervals [20, 54] km and [-24, 54] km, respectively.

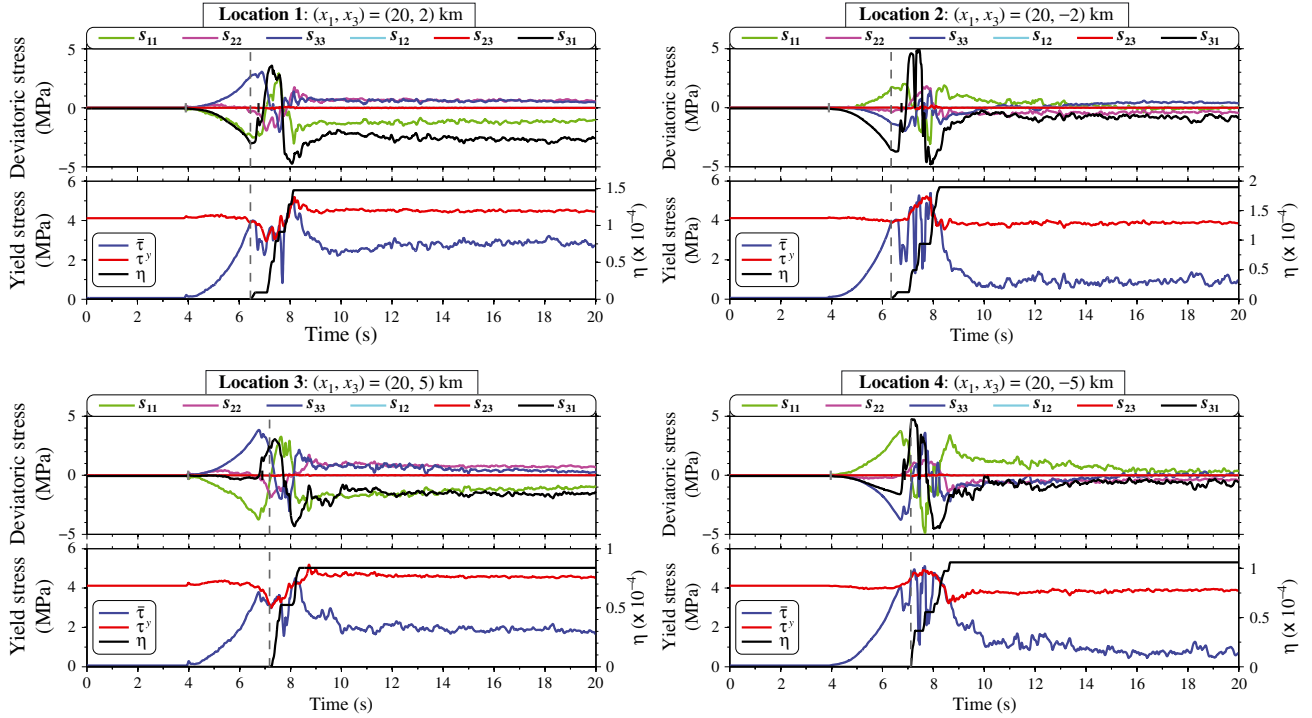


Figure 15. Time histories of deviatoric stress components (s_{ij}), yield stress ($\bar{\tau}$ and τ^y), and accumulated plastic strain (η) at Locations 1–4 indicated in Figure 13. The gray and black ticks marked in the deviatoric stress plots denote the hypocentral P and S arrivals, respectively; the gray dashed vertical line marks the initial occurrence of plastic yielding.

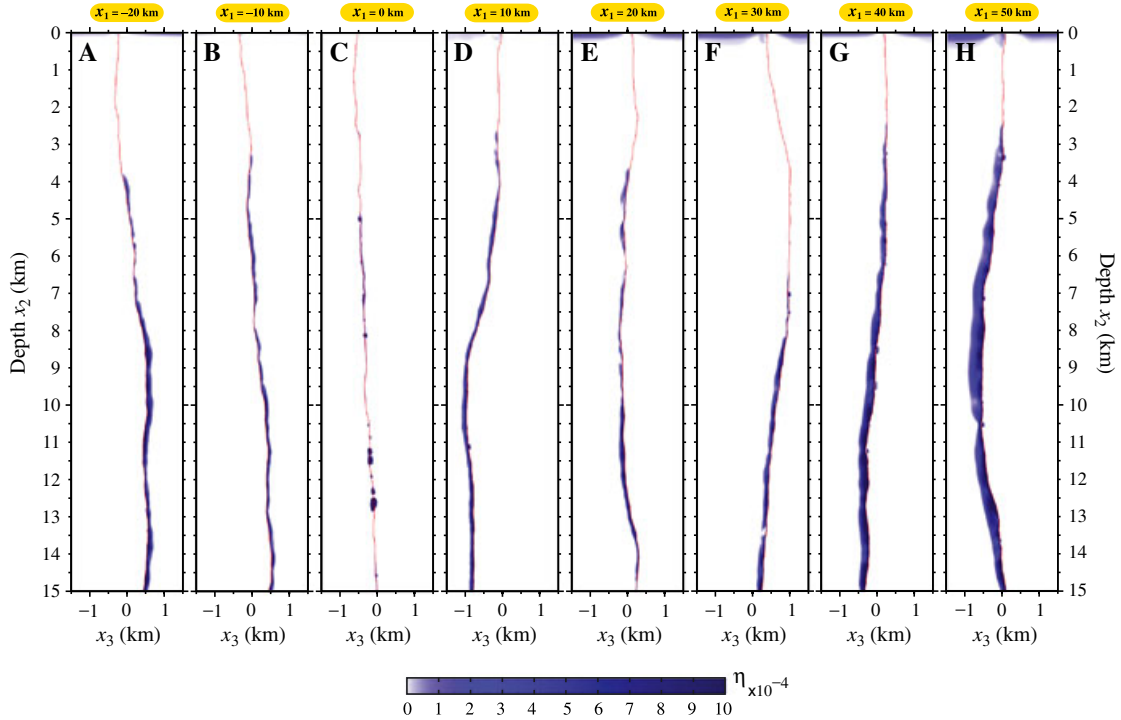


Figure 16. Cross-section views of plastic deformation at various along-strike (x_1) distances showing the along-depth distribution of η .

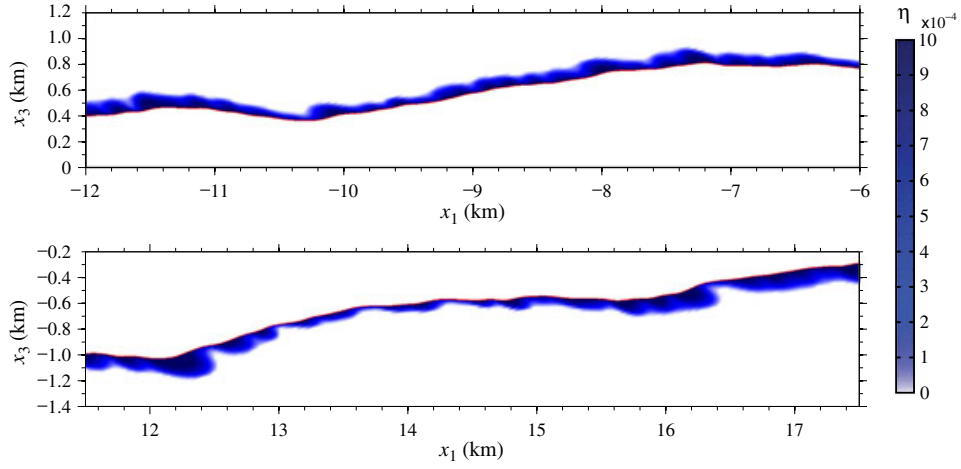


Figure 17. Close-up map views of plastic deformation around the fault along different fault sections at the hypocentral depth of 12 km. Plastic deformation is mainly concentrated on the extensional side of the fault.

median curves hereafter. The four plots in Figure 22 are for periods of 0.1, 0.3, 1.0, and 3.0 s, respectively. The dashed curves are the GMPE median curves, i.e., for a median site and median event, for the same magnitude as the simulated event ($M_w=7.23$). The shaded regions indicate the range

of the four predictions for an 84th percentile event, i.e., median plus one standard deviation of the inter-event component of variability τ [Brillinger and Preisler, 1984, 1985]. The intra-event component of empirical variability (denoted by ϕ in the notation recommended by Al Atik et al. [2010]) is

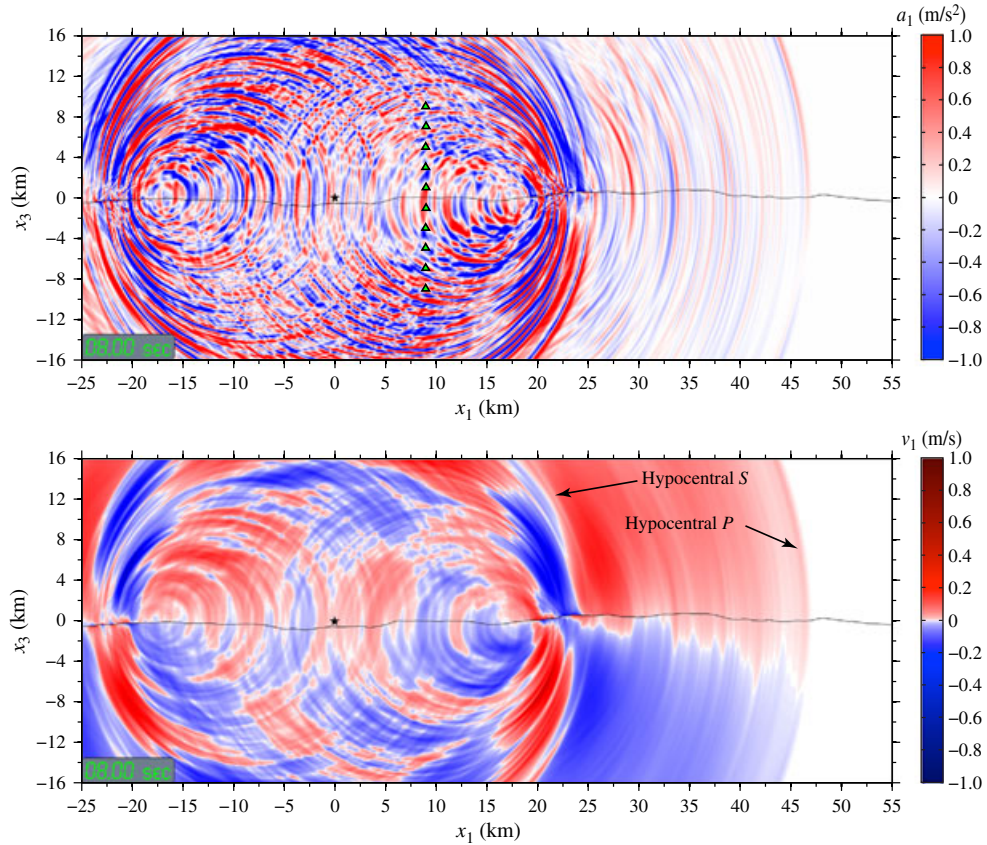


Figure 18. Snapshots of the fault-parallel (top) acceleration and (bottom) velocity fields at the free surface at time $t=8$ s. Epicenter is indicated by a star symbol. The three-component accelerograms at stations marked by green triangles in the top plot at $x_1=9$ km are shown in Figure 19. The hypocentral P and S waves are labeled.

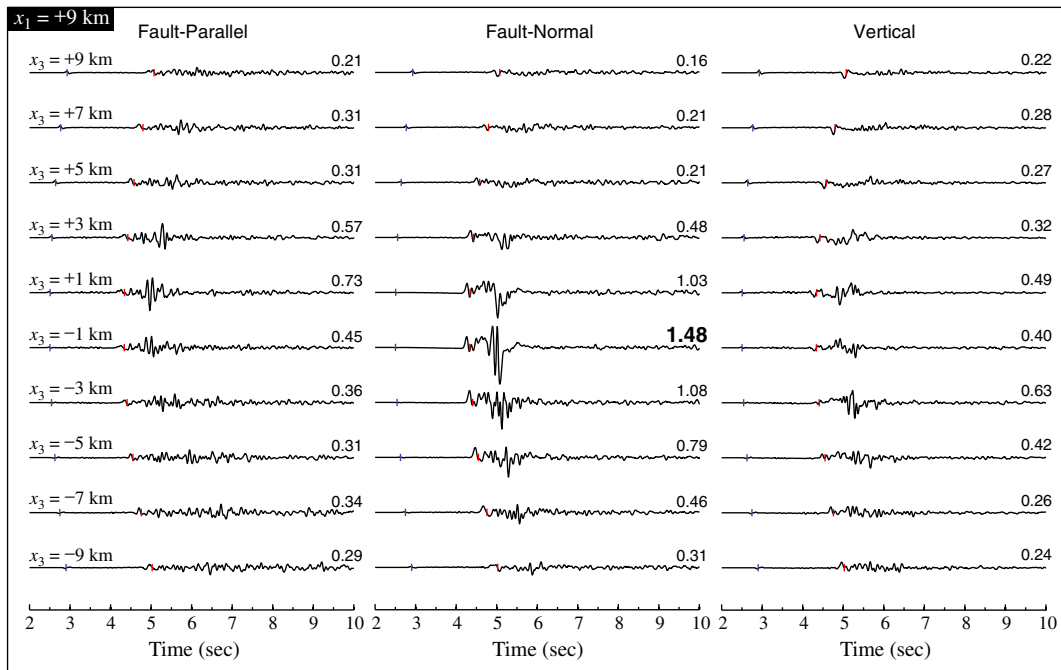


Figure 19. Low-pass filtered (<15 Hz) three-component accelerograms at surface stations at $x_1 = 9$ km indicated in Figure 18. The peak amplitude of each record in unit of g is labeled on top. The fault-normal accelerogram at $x_3 = -1$ km has the largest peak amplitude of 1.48 g . The hypocentral P and S arrivals on each accelerogram are labeled blue and red vertical dashes, respectively. Fourier power spectra of the accelerograms at $x_3 = 1$ km are shown in Figure 20a.

excluded by the within-event averaging operation performed on the simulated ground motion.

[37] The shape (distance dependence) of each simulation median curve in Figure 22 is similar to its empirical counterpart. Except for the case of 1.0 s period, the two are indistinguishable within the epistemic uncertainty of the empirical medians. The absolute levels of the simulation median curves are also consistent with empirical estimates for an 84th percentile event, and there is no obvious bias in the period dependence between simulation and empirical curves. Ground-motion results from another rough-fault simulation in which we replace the uniform velocity model with a 1D-layered velocity model (LOHS1 in *Dreger and Helmberger* [1991]) show similar comparability between the simulation median curve and its empirical counterpart.

4. Discussion

[38] Through 3-D numerical simulations, we demonstrate that fault roughness can play a significant role in the dynamic rupture process and resultant ground-motion excitation. The numerical calculations in this study employ a rate-and-state friction with a strongly rate-weakening response, combined with regularized normal traction dependence. Bulk response is represented by Drucker-Prager elastoplasticity (with viscous regularization), permitting relaxation of excessive stress concentrations induced around the roughness slopes in the dynamic process. The fault roughness assumed in our model is self-similar over three orders of magnitude in length scale, from $\sim 10^2$ to $\sim 10^5$ m. In this section, we extend the discussion of our model results in an effort to establish some potential

connections to seismic and geological observables. Some model limitations will be also discussed.

[39] Simulations in this study suggest several potentially observable effects of fault roughness. One example is slip-pulse duration, which has been inferred for many events from seismic observations. Previous theoretical studies [e.g., *Zheng and Rice*, 1998] have shown that strongly rate-weakening friction leads to pulse-like rupture along a planar interface when background stress is close to a critical level. Along a rough fault, sensitivity of the rupture properties to the level of background stress is even greater. The presence of fault roughness causes local stress perturbations that, in general, promote self-healing and introduce incoherence in the rupture process. These effects from fault roughness increase with increasing degree of roughness (decreasing λ_{\min} and/or increasing α). In the cases we examined, the influence of roughness on the rupture fronts is relatively modest, but the influence on the trailing healing front is stronger. The degree of influence apparently depends on many factors, including background stress, roughness parameters, friction parameters, and even plasticity parameters. For example, with similar friction law and off-fault plasticity, *Dunham et al.* [2011b] in their 2-D simulations observed much larger fluctuations of rupture front speed with $\Psi = 50^\circ$ than with $\Psi = 20^\circ$, where Ψ is the angle of the maximum principal prestress to the mean fault line.

[40] A second potentially observable consequence is short-wavelength fluctuation of surface slip. In the rough-fault simulations, surface-slip fluctuations on the order of several tens of percent are present over length scales of a few hundred meters. This level and scale of fluctuation is at least qualitatively similar to results emerging from recent high-resolution

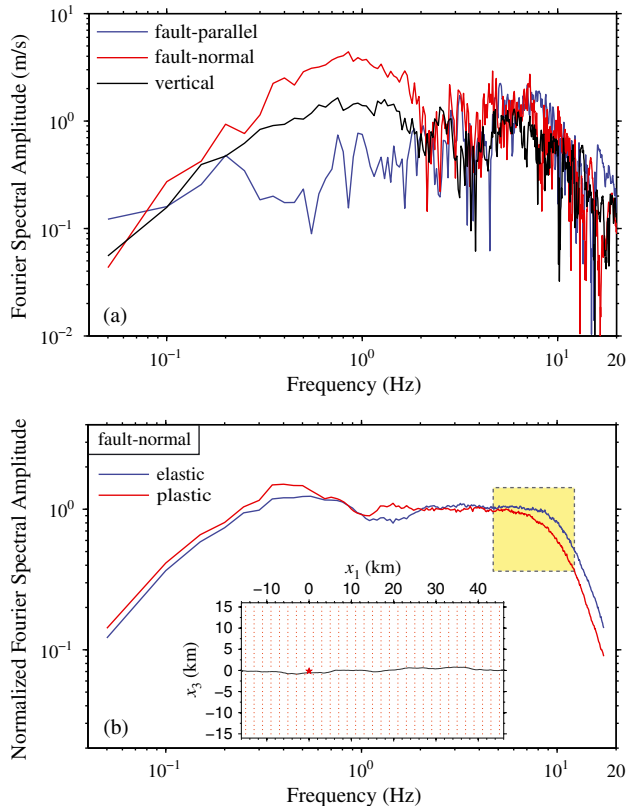


Figure 20. (a) Fourier spectra of the three-component accelerograms at surface station $(x_1, x_3) = (9, 1)$ km. (b) Normalized Fourier spectra of the fault-normal accelerograms (averaged over surface stations at locations indicated in the inset) from simulations with and without off-fault plasticity. Each Fourier spectrum is individually normalized to unit mean Fourier amplitude between 1 and 5 Hz before averaging. The shift of upper cutoff frequency f_{\max} is highlighted in a dashed yellow box.

imaging studies of displacements near earthquake surface ruptures. For example, *Rockwell et al.* [2002] and *Rockwell and Klinger* [2013] report slip fluctuations of 30% or more over lateral distances of a kilometer or less, for both the Izmit (Turkey) and the 1940 Imperial Valley (California) ruptures. At a larger scale (~ 20 km), *Klinger et al.* [2006] found that slip variations for the 2001 Kokoxili (Tibet) earthquake correlate with along-strike geometrical perturbations of the fault trace. The extent to which observed heterogeneity of surface displacement fields at various scales can be actually attributed to fault geometrical roughness remains uncertain but might be illuminated by more quantitative comparisons between observed displacement images and rough-fault simulations. Such comparisons could include examination of the spectral characteristics of observed and simulated surface ruptures, as well as assessments of the degree (and sign) and scale dependence of any correlation between slip fluctuation and local fault trace orientation.

[41] Some characteristics of the simulated inelastic zone may also have observable consequences. Figures 16 and 17 show that, in the presence of fault roughness, inelastic strain accumulation is concentrated in an irregular zone with a thickness varying between zero and several hundred meters. These heterogeneities in the degree of inelastic strain accumulation are associated with local topographic features of the fault (or frictional properties, in the case of the velocity-strengthening zone). Assuming that those geometrical features (or frictional properties) are long-lived, and that the inelastic response in our model is a rough predictor of damage accumulation (at least over some depth range), we would also expect the distribution of rupture-induced damage from multiple earthquakes to reflect a similar spatial heterogeneity. The existence of spatial heterogeneity at the scale of a few kilometers is consistent with the observations of *Lewis and Ben-Zion* [2010], who inferred from seismic observations that waveguide effects attributable to fault zone damage along the

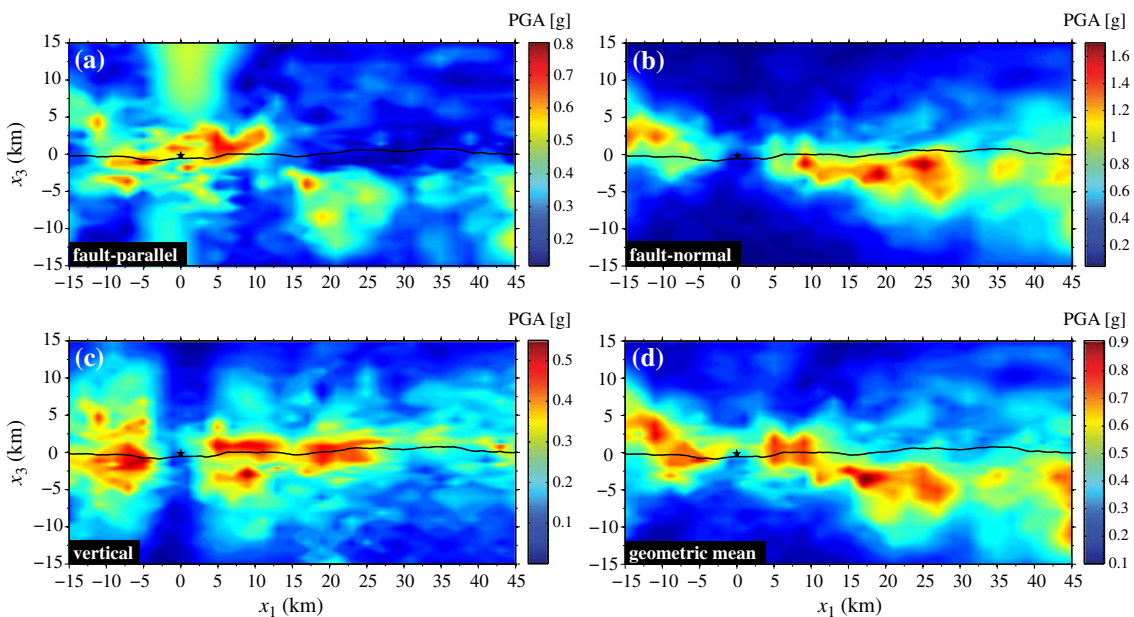


Figure 21. Patterns of (a) fault-parallel, (b) fault-normal, (c) vertical, and (d) geometric mean PGA from the simulation with a rough fault. The fault trace and epicenter are indicated.

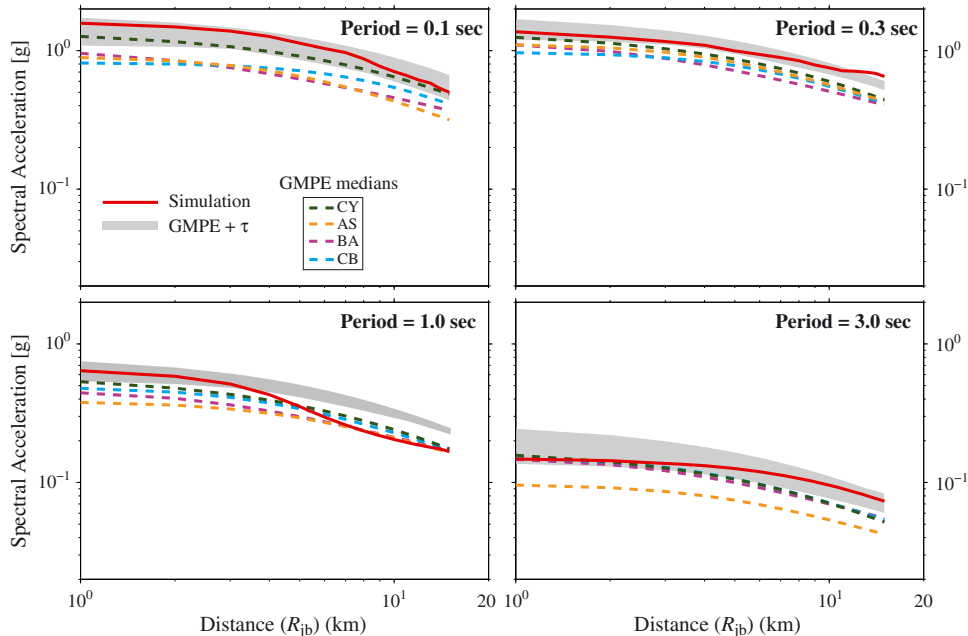


Figure 22. Comparison of median response spectra from the simulation (red solid curves) with four GMPE median curves (dashed curves) for four different periods: 0.1, 0.3, 1, and 3 s. Gray shading indicates the range of the GMPEs for the median plus τ (the inter-event standard deviation) prediction.

Parkfield section of the San Andreas Fault are likewise very heterogeneous, with trapped wave observations typically limited only to stations within a few kilometers of the source events.

[42] Our simplified model only includes inelastic shear strain, but we would expect the actual expression of inelastic response at shallow depth to have a comparably large volumetric component as well. *Replogle* [2011] has documented anomalously high volumetric strains in saprock within ~ 5 km of the Elsinore Fault in southern California (on the order of several tens of percent) compared with background levels found at their reference site at ~ 15 km distance. They interpreted these strains as a signature of accumulated coseismic damage induced by ground motion from repeated large earthquakes. The extensive near-surface inelastic strain distribution from our simulations is consistent with that interpretation.

[43] We showed that synthetic ground-motion intensity measures from our rough-fault simulations are statistically similar in their site-averaged median predictions to those of GMPEs that aggregate information from a large number of recordings from many events and sites (Figure 22). The within-event standard deviations, i.e., the standard deviations of the natural logarithm of the residual after removal of the simulation median at each distance, are also of interest, highlighting additional observational issues. The standard deviations calculated from the simulation results are lower than their empirical counterparts, i.e., the intra-event standard deviations of the GMPE residuals. This result is expected, since our uniform half-space (and also 1D-layered velocity) models have introduced none of the site and path effects that contribute variability to empirical ground motions. However, several recent studies have demonstrated that a substantial component of the empirical intra-event variance ϕ^2 is attributable to site- and path-specific terms that are fixed effects that can be estimated (along with event terms) when a sufficient number

of earthquake records from multiple events are available at a common set of sites. Residual standard deviation after correction for these reproducible path and site effects, i.e., the within-event single-path standard deviation (denoted by $\phi_{0,B}$ in the nomenclature of *Al Atik et al.* [2010]), is significantly smaller than the conventional standard deviation estimated from aggregated data for multiple (uncorrected) stations and paths. A large portion of the reported estimates of $\phi_{0,B}$ (or very similar measures of variability) in recent studies are in the range 0.35 ± 0.1 with little period dependence (at least for period up to ~ 1 s) [e.g., *Atkinson*, 2006; *Morikawa et al.*, 2008; *Lin et al.*, 2011; *Rodriguez-Marek et al.*, 2011; *Anderson and Uchiyama*, 2011].

[44] If we conjecture that the within-event single-path standard deviation is principally the result of random interferences among multiple wavefronts, we might expect the intra-event standard deviation from simulations such as ours—with a complex source, but without distinct site or path effects—to be comparable to the empirical estimates of $\phi_{0,B}$ cited in the previous paragraph. For the simulation with the uniform half-space model, the standard deviation (averaged for 0.1, 0.3, 1.0, and 3.0 s spectral ordinates) is 0.35; for the simulation with the 1D-layered velocity model, the corresponding averaged standard deviation is 0.23. These values are remarkably similar to the empirical single-path sigma values. It will be informative in the future to see how stable the variability is over a large suite of such simulations and how sensitive it is to the addition of a spatially stationary stochastic component to the seismic velocity model.

[45] One notable limitation of the study is the employed simplification of the initial stress tensor field. By excluding lateral heterogeneity in the model stress field, we are able to isolate and therefore more easily interpret the effects of fault roughness, but in the meantime, we are left with uncertainties about how those effects may be modulated by

realistic stress heterogeneities. A more self-consistent model should include the inevitable heterogeneities in the volumetric stress field surrounding the fault generated by multiple earthquakes (e.g., Figure 8); and it is not realistic to assume full relaxation of these heterogeneities prior to each subsequent rupture event. In addition, the shallow slip deficit resulting from the simulated single rupture event in this study (Figure 9) is not sustainable over multiple earthquake cycles. The upper friction transition layer from velocity weakening to velocity strengthening, abetted by the assumption of simplified initial stress field, is responsible for the general deficiency of fault slip at depth < 4 km. The resultant slip deficiency in turn suppresses plastic deformation at these shallow depths, a result that is unlikely to be general and commonly observed along major faults in nature.

[46] Further work is needed to explore the dependence of ground motion on the level of average background shear stress. Our simulated event produced response spectral predictions at about the level of a median-plus-sigma earthquake, suggesting that we could lower the background shear stress to simulate a median event (or, more generally, vary the stress level over some probability distribution to generate an event ensemble with the statistics of real events). In our preliminary efforts to do so, we have found that most model events nucleated at the same hypocenter, but with a lower background shear stress, fail to grow to system-size events (i.e., events approaching the full available fault dimension and target magnitude), instead stopping at smaller magnitude. Thus, a comprehensive sensitivity study of ground motion to background stress level (at a given event magnitude) may require extensive experimentation, involving many random realizations of the roughness model and many trial hypocenters. Furthermore, previous work in 2-D [Dunham *et al.*, 2011b] has shown that the rupture process becomes very sensitive to the background stress level when that level approaches the minimum that permits self-sustaining rupture. The smoothness of the rupture-time contours in our model may indicate that we are operating, to some extent, above that minimum, which would be consistent with the fact that predicted ground motion is somewhat above that of a median event of the same magnitude.

[47] Another important issue that remains to be investigated is the combined effect of multiple physical length scales and processes in the model on f_{\max} . As noted in section 3.3, we have found that, in addition to the off-fault plastic deformation process, f_{\max} is sensitive to the minimum roughness wavelength λ_{\min} and the rupture cohesive zone size Λ that scales with state evolution slip L . A separate factor-of-two change in either λ_{\min} or L induces a shift in f_{\max} of similar magnitude to that attributable to the plastic yielding (Figure 20b). A parameter-space study to fully quantify these effects on f_{\max} will be complicated by the fact that those effects are nonlinear and strongly coupled. For example, reduction of L tends to increase high-frequency radiation by downscaling the cohesive zone dimension, but that in turn induces more near-fault inelastic deformation that limits the contraction of the cohesive zone [Day *et al.*, 2005; Duan and Day, 2008; Hok *et al.*, 2010], and thus counteracts the associated increase of f_{\max} . We can expect similar effects on f_{\max} from changes to λ_{\min} . Interpretation of the current results is further limited by the fact that, given our input parameters, the associated length scales affecting f_{\max} (i.e., minimum cohesive zone dimension

Λ_{\min} , minimum roughness wavelength λ_{\min} , and width of plastic deformation zone) are all of roughly the same size, on the order of 100 m, and near our numerical resolution limit.

5. Conclusions

[48] It is now feasible to perform large-scale 3-D simulations of dynamic rupture along faults with self-affine geometrical complexity spanning more than three orders of magnitude in scale length. The corresponding near-fault seismic wavefield from ruptures with length on the order of 100 km can be modeled up to frequencies of approximately 10 Hz. Our rough-fault models accounting for strongly rate-dependent friction and off-fault inelastic yielding predict potentially observable dynamic effects of fault roughness on the time dependence and spatial variability of slip and on the distribution of near-fault damage. These effects may provide at least partial explanation for some recent results from high-resolution imaging of fault zones, including large kilometer-scale variations in surface slip, large cumulative volumetric strains in the near surface several kilometers removed from the fault trace, and large variability of the thickness and continuity of fault damage zones on the scale of several to tens of kilometers.

[49] Synthetic response spectra show median distance and period dependence, absolute level, and intra-event standard deviation that are remarkably similar to appropriate empirical estimates throughout the period range 0.1–3.0 s. This statistical similarity indicates that even in its current incomplete form (with highly simplified initial stress conditions), the rough-fault model constitutes a potentially useful parameterization of ground-motion generation processes over a wide frequency range, much of which is of great engineering interest. Simulations based on similar models may prove useful, both for incorporating known source- and/or path-specific effects into ground-motion estimates and for elucidating generic aspects of ground motion that are still poorly defined by existing data. The latter include effects on ground-motion intensity measures due to seismic directivity, near-fault static displacements, and hanging-wall amplifications in the case of reverse and normal events. More elaborate simulations, with the addition of stochastic heterogeneities to the wave speed and density of the media, may further offer improved quantitative understanding of the source, site, and path origins of variability in ground-motion intensity measures, along with estimates of the extent to which standard deviations of empirical estimation procedures may be reduced by site- and path-specific observational studies.

Appendix A: Self-Similar Fault Surface

[50] A self-affine 1-D profile $z(x)$ remains statistically invariant under scaling transformation $(x, z) \rightarrow (\lambda x, \lambda^H z)$. The exponent H is typically referred to as the *Hurst exponent* or *roughness index* with its value ranging between 0 and 1. A self-similar 1-D profile can be regarded as a special case with $H=1$ such that it remains statistically identical with transformation $(x, z) \rightarrow (\lambda x, \lambda z)$. Therefore, a magnified portion of a self-similar profile appears statistically identical to the whole if the same magnification factor is applied in both x and z directions. In contrast, different magnification factors in each direction are needed for a magnified portion of a self-affine profile to appear statistically unchanged from the whole. In real-world physical situations, self-similarity is typically

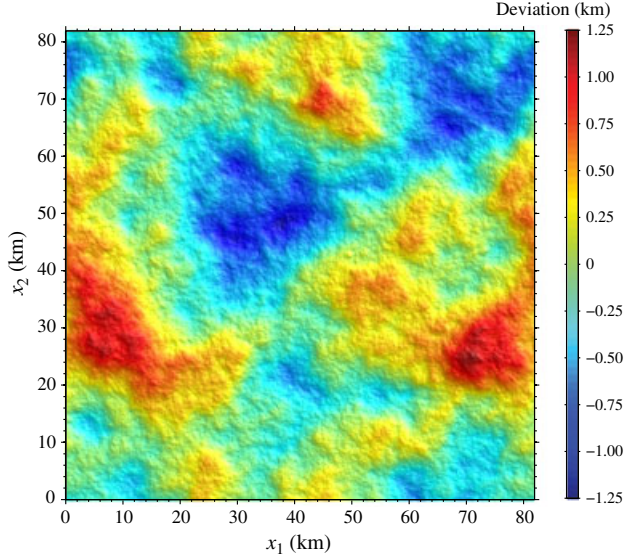


Figure A1. A representative synthetic 2-D band-limited self-similar roughness distribution with $\lambda_{\min} = 80$ m and $\alpha = 10^{-2.3}$. The color scale denotes the roughness deviations from the mean plane.

valid only over a limited range of length scales, of which the lower and upper boundaries are denoted here by λ_{\min} and λ_{\max} , respectively.

[51] The Fourier power spectrum of a 1-D self-affine profile has a power law form $P(k) \propto k^{-\beta}$ with $\beta = 2H + 1$, which, when plotted as a function of wave number k in log-log scale, has a linear slope of $-(2H + 1)$. In particular, the power spectrum of a 1-D self-similar profile should have a linear slope of -3 ($H = 1$). Statistical methods for fractal 1-D profiles can be applied to the examination of self-affine or self-similar 2-D functions by analyzing parallel 1-D profiles extracted from them in all directions [e.g., *Candela et al.*, 2009]. In particular, due to the isotropic nature of self-similarity in all directions, an extracted 1-D profile can be an excellent approximate of the whole in terms of roughness statistics.

[52] A 2-D self-similar topography has a power spectral density that is of the same form, $k^{-\beta}$, where $k = (k_1^2 + k_2^2)^{1/2}$, with k_1 and k_2 being the wave numbers in two orthogonal directions, and exponent $\beta = 2H + 2$. The power spectra of 1-D profiles extracted from the 2-D function, however, will still have a linear slope of $-(2H + 1)$ on a log-log plot. Self-similar 2-D rough-fault surfaces in this study are generated by using the Fourier transform method [Andrews and Barall, 2011]. First, a square array of complex numbers is generated with the real and imaginary parts being pairs of independent normal random variables obtained using the polar method [Marsaglia and Bray, 1964]. These complex numbers are a representation of the rough surface in the wave number domain. Next we multiply the complex numbers by the desired amplitude spectrum that corresponds to a 2-D self-similar distribution, i.e., $k^{-\beta/2}$ or $(k_1^2 + k_2^2)^{-1}$. A Butterworth low-pass filter is then applied to the square array to eliminate the short-wavelength roughness components that are beyond the resolution of our computation. Finally, an inverse Fourier transform is performed on the square complex array to obtain a band-limited self-similar 2-D profile. The resultant square array is cropped

in the coordinate direction that corresponds to depth to make it agree with the rectangular shape of the fault suitable for numerical simulations.

[53] The procedure described above only prescribes how the surface roughness changes with wavelength as a self-similar distribution. An additional parameter is required to control the steepness or total variance of the fault-surface topography [Power and Tullis, 1991]. To that end, we introduce the amplitude-to-wavelength ratio α defined as

$$\alpha = h_{\text{rms}}/L \quad (\text{A1})$$

where L is the total length of the fault in the along-strike direction and h_{rms} is the rms roughness of the 2-D profile $h(n_1, n_2)$ given by

$$h_{\text{rms}} = \left\{ \frac{1}{N_1 N_2} \sum_{n_2=0}^{N_2-1} \sum_{n_1=0}^{N_1-1} [h(n_1, n_2) - \bar{h}]^2 \right\}^{1/2} \quad (\text{A2})$$

$$\bar{h} = \frac{1}{N_1 N_2} \sum_{n_2=0}^{N_2-1} \sum_{n_1=0}^{N_1-1} h(n_1, n_2) \quad (\text{A3})$$

where n_1 and n_2 denote the 2-D grid of the fault surface with $0 \leq n_1 \leq N_1 - 1$ and $0 \leq n_2 \leq N_2 - 1$. By self-similarity, α is scale invariant: if h'_{rms} results from applying (A2) to a subset of the fault of length L' , a fixed ratio is maintained, i.e., $h'_{\text{rms}}/L' = h_{\text{rms}}/L = \alpha$.

[54] The minimum value of λ_{\min} appropriate for numerical simulations is dictated by two conditions. The first condition relates to the computational grid spacing: the shortest roughness wavelength has to be sampled sufficiently so that the wavefield irregularities induced are numerically resolvable. The second condition relates to the largest fault slip generated in the model: since our formulation neglects geometrical nonlinearities, there is an implicit assumption that slip is small compared with the shortest roughness wavelength, so that the geometric relationship between the two faces of the fault does not change appreciably during fault slip.

[55] Figure A1 shows a synthetic 2-D self-similar roughness distribution randomly generated using the Fourier transform method described above, with $\lambda_{\min} = 80$ m and $\alpha = 10^{-2.3}$. The power spectra of 1-D profiles extracted from the 2-D roughness pattern all show spectral slopes indicative of self-similarity in wavelength range $[\lambda_{\min}, \lambda_{\max}]$ as designed (Figure A2).

Appendix B: RSD Friction With Regularized Normal Traction Dependence

[56] The frictional behavior of the fault interface is characterized by an RSD friction with a strongly rate-weakening feature combined with a regularized normal traction response. The vectors of shear traction \mathbf{T}_s and slip velocity \dot{s} are parallel, satisfying

$$\mathbf{T}_s |\dot{s}| = |\mathbf{T}_s| \dot{s} \quad (\text{B1})$$

with the magnitude of the shear traction given by

$$|\mathbf{T}_s| = f(V, \psi) \theta_{\text{PC}} \quad (\text{B2})$$

where $f(V, \psi)$ is the friction coefficient as a function of slip

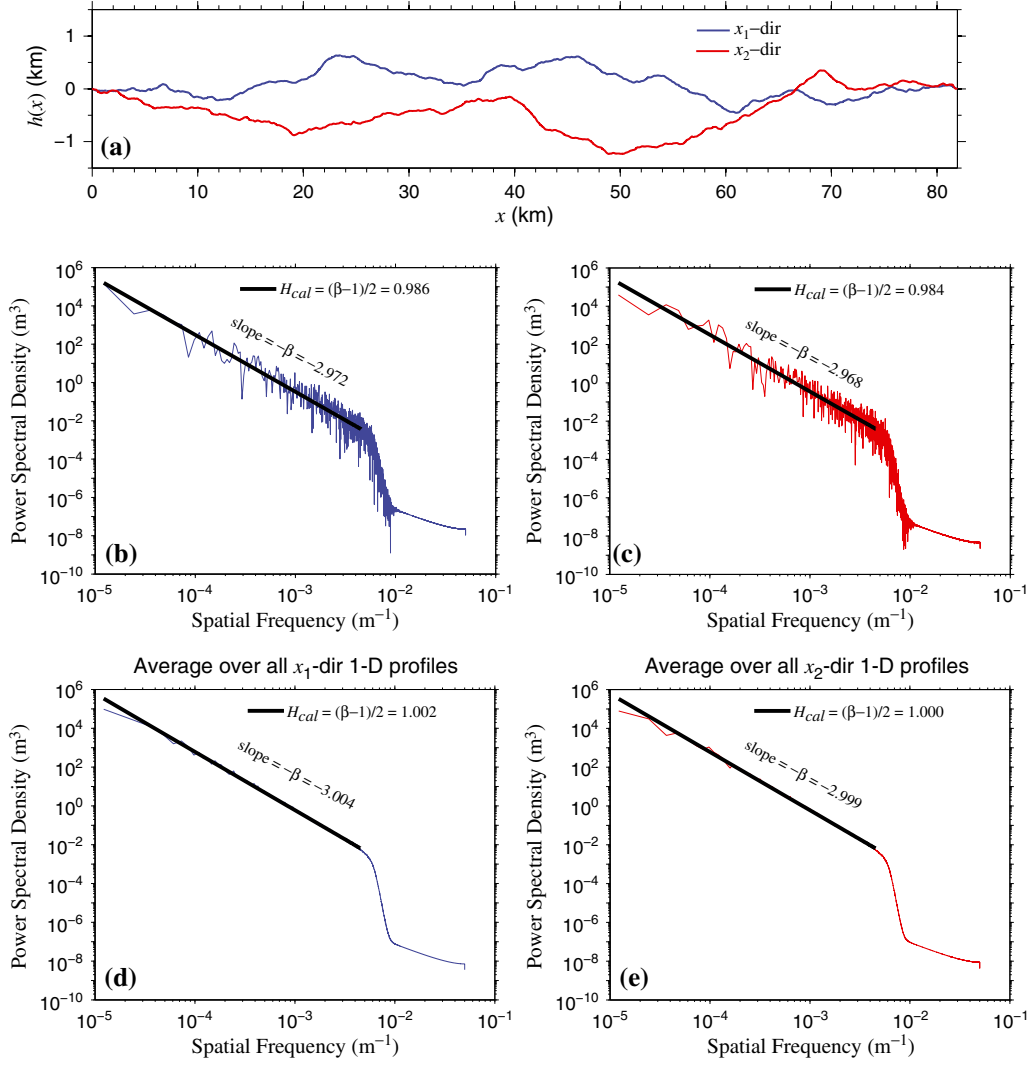


Figure A2. (a) Line profiles randomly extracted from the 2-D roughness pattern in Figure A1 along two orthogonal directions: parallel to x_1 and x_2 axes. The Fourier power spectra of these two line profiles are shown in (b) and (c), respectively. (d and e) The average Fourier power spectra for all the lines parallel to x_1 and x_2 axes, respectively. All of the power spectra roll off sharply beyond the wave number that corresponds to λ_{\min} . The values of Hurst number H_{cal} estimated from the slopes of power spectra (b–e) in the designed wavelength range are all very close to the self-similarity value of 1.

speed V and friction state variable ψ , and θ_{PC} is a second state variable that has steady-state value equal to the normal traction T_n .

[57] The RSD friction coefficient can be expressed in a regularized form [Rice, 1983, 2006; Noda *et al.*, 2009; Dunham *et al.*, 2011a] as

$$f(V, \psi) = a \sinh^{-1} \left[\frac{V}{2V_0} \exp\left(\frac{\psi}{a}\right) \right] \quad (\text{B3})$$

where the evolution of state variable ψ follows a slip law

$$\dot{\psi} = -\frac{V}{L} [\psi - \psi_{ss}(V)] \quad (\text{B4})$$

$$\psi_{ss}(V) = a \ln \left\{ \frac{2V_0}{V} \sinh \left[\frac{f_{ss}(V)}{a} \right] \right\}. \quad (\text{B5})$$

[58] The function f_{ss} in equation (B5) can be interpreted as a steady-state coefficient of friction. Following Noda *et al.* [2009], $f_{ss}(V)$ takes the form given by

$$f_{ss}(V) = f_w + \frac{f_{LV}(V) - f_w}{\left[1 + (V/V_w)^8 \right]^{1/8}}. \quad (\text{B6})$$

[59] The above form has a strongly velocity-weakening feature such that when $V \gg V_w$, f_{ss} approaches a fully weakened friction coefficient f_w , approximating experimental observations of frictional weakening at high slip speed [e.g., Beeler *et al.*, 2008]. When $V \ll V_w$, f_{ss} approaches a low-velocity steady-state friction coefficient, i.e.,

$$f_{LV}(V) = f_0 - (b - a) \ln(V/V_0). \quad (\text{B7})$$

[60] Frictional sliding experiments with variable normal stress show that the shear strength responds gradually to abrupt changes of normal stress [e.g., Prakash and Clifton, 1993; Prakash, 1998]. We account for that experimental

observation by using the state variable θ_{PC} in the calculation of shear traction in (B2), instead of the normal traction T_n , where the evolution of θ_{PC} is given by

$$\dot{\theta}_{PC} = -\frac{V}{L_{PC}}[\theta_{PC} - |T_n|]. \quad (\text{B8})$$

[61] Table 1 contains the definitions of friction parameters a , b , f_0 , f_w , V_0 , V_w , L , and L_{PC} , along with their values used in simulations.

[62] **Acknowledgments.** We thank Geoffery P. Ely for advice and assistance in the use of SORD. We also benefited from helpful suggestions from two anonymous referees and Editor Robert Nowack. The simulations were performed on a Cray XT5 (Kraken) at the National Institute for Computational Sciences. This work was supported by the National Science Foundation (NSF) Awards EAR-0810271, EAR-1135455, EAR-949443 (PetaSHA3), and OCI-0905019 (PetaShake2) and by the Southern California Earthquake Center (SCEC). SCEC is funded by NSF Cooperative Agreement EAR-0529922, USGS Cooperative Agreement 07HQAG0008. The SCEC contribution number for this article is 1672.

References

- Abrahamson, N. A., and W. Silva (2008), Summary of the Abrahamson & Silva NGA ground-motion relations, *Earthq. Spectra*, *24*(1), 67–97, doi:10.1193/1.2924360.
- Al Atik, L., N. A. Abrahamson, J. J. Bommer, F. Scherbaum, F. Cotton, and N. Kuehn (2010), The variability of ground-motion prediction models and its components, *Seismol. Res. Lett.*, *81*(5), 794–801, doi:10.1785/gssrl.81.5.794.
- Anderson, J. G., and S. E. Hough (1984), A model for the shape of the Fourier amplitude spectrum of acceleration at high frequencies, *Bull. Seismol. Soc. Am.*, *74*(5), 1969–1993.
- Anderson, J. G., and Y. Uchiyama (2011), A methodology to improve ground-motion prediction equations by including path corrections, *Bull. Seismol. Soc. Am.*, *101*(4), 1822–1846, doi:10.1785/0120090359.
- Andrews, D. J. (2005), Rupture dynamics with energy loss outside the slip zone, *J. Geophys. Res.*, *110*, B01307, doi:10.1029/2004JB003191.
- Andrews, D. J., and M. Barall (2011), Specifying initial stress for dynamic heterogeneous earthquake source models, *Bull. Seismol. Soc. Am.*, *101*, 2408–2417, doi:10.1785/0120110012.
- Atkinson, G. M. (2006), Single-station sigma, *Bull. Seismol. Soc. Am.*, *96*(2), 446–455, doi:10.1785/0120050137.
- Beeler, N. M., T. E. Tullis, and D. L. Goldsby (2008), Constitutive relationships and physical basis of fault strength due to flash heating, *J. Geophys. Res.*, *113*, B01401, doi:10.1029/2007JB004988.
- Ben-Zion, Y., and C. G. Sammis (2003), Characterization of fault zones, *Pure Appl. Geophys.*, *160*, 677–715, doi:10.1007/PL00012554.
- Ben-Zion, Y., and Z. Shi (2005), Dynamic rupture on a material interface with spontaneous generation of plastic strain in the bulk, *Earth Planet. Sci. Lett.*, *236*, 486–496, doi:10.1016/j.epsl.2005.03.025.
- Bistacchi, A., W. A. Griffith, S. A. F. Smith, G. Di Toro, R. Jones, and S. Nielsen (2011), Fault roughness at seismicogenic depths from LIDAR and photogrammetric analysis, *Pure Appl. Geophys.*, doi:10.1007/s00024-011-0301-7.
- Boore, D. M., and G. M. Atkinson (2008), Ground-motion prediction equations for the average horizontal component of PGA, PGV, and 5%-damped PSA at spectral periods between 0.01 s and 10.0 s, *Earthq. Spectra*, *24*(1), 99–138, doi:10.1193/1.2830434.
- Boore, D. M., and W. B. Joyner (1978), The influence of rupture incoherence on seismic directivity, *Bull. Seismol. Soc. Am.*, *68*, 283–300.
- Boore, D. M., and W. B. Joyner (1997), Site amplifications for generic rock sites, *Bull. Seismol. Soc. Am.*, *87*(2), 327–341.
- Boore, D. M., J. Watson-Lamprey, and N. A. Abrahamson (2006), Orientation-independent measures of ground motion, *Bull. Seismol. Soc. Am.*, *96*(4A), 1502–1511, doi:10.1785/0120050209.
- Brillinger, D. R., and H. K. Preisler (1984), An exploratory analysis of the Joyner-Boore attenuation data, *Bull. Seismol. Soc. Am.*, *74*(4), 1441–1450.
- Brillinger, D. R., and H. K. Preisler (1985), Further analysis of the Joyner-Boore attenuation data, *Bull. Seismol. Soc. Am.*, *75*(2), 611–614.
- Bryant, W. A. (Comp.) (2005), Digital database of Quaternary and younger faults from the fault activity map of California, version 2.0, California Geological Survey. [Available at http://www.consrv.ca.gov/CGS/information/publications/Pages/QuaternaryFaults_ver2.aspx.]
- Campbell, K. W. (2003), Prediction of strong ground motion using the hybrid empirical method and its use in the development of ground-motion (attenuation) relations in eastern North America, *Bull. Seismol. Soc. Am.*, *93*(3), 1012–1033, doi:10.1785/0120020002.
- Campbell, K. W., and Y. Bozorgnia (2008), NGA ground motion model for the geometric mean horizontal component of PGA, PGV, PGD and 5% damped linear elastic response spectra for periods ranging from 0.01 to 10 s, *Earthq. Spectra*, *24*(1), 139–171, doi:10.1193/1.2857546.
- Campillo, M., P. Favreau, I. R. Ionescu, and C. Voisin (2001), On the effective friction law of a heterogeneous fault, *J. Geophys. Res.*, *106*(B8), 16,307–16,322.
- Candela T., F. Renard, M. Bouchon, A. Brouste, D. Marsan, J. Schmittbuhl, and C. Voisin (2009), Characterization of fault roughness at various scales: Implications of three-dimensional high resolution topography measurements, *Pure Appl. Geophys.*, *166*, 1817–1851, doi:10.1007/s00024-009-0521-2.
- Candela, T., F. Renard, Y. Klinger, K. Mair, J. Schmittbuhl, and E. E. Brodsky (2012), Roughness of fault surfaces over nine decades of length scales, *J. Geophys. Res.*, *117*, B08409, doi:10.1029/2011JB009041.
- Chester, F. M., and J. S. Chester (2000), Stress and deformation along wavy frictional faults, *J. Geophys. Res.*, *105*, 23,421–23,430.
- Chiou, B. S.-J., R. Darragh, N. Gregor, and W. Silva (2008), NGA project strong-motion database, *Earthq. Spectra*, *24*(1), 23–44, doi:10.1193/1.2894831.
- Chiou, B. S.-J., and R. Youngs (2008), An NGA model for the average horizontal component of peak ground motion and response spectra, *Earthq. Spectra*, *24*(1), 173–215, doi:10.1193/1.2894832.
- Day, S. M., L. A. Dalgner, N. Lapusta, and Y. Liu (2005), Comparison of finite difference and boundary integral solutions to three-dimensional spontaneous rupture, *J. Geophys. Res.*, *110*(B12), 1–23, doi:10.1029/2005JB003813.
- Dieterich, J. H., and D. E. Smith (2009), Nonplanar faults: Mechanics of slip and off-fault damage, *Pure Appl. Geophys.*, *166*, 1799–1815, doi:10.1007/s00024-009-0517-y.
- Di Toro, G., D. L. Goldsby, and T. E. Tullis (2004), Friction falls toward zero in quartz rock as slip velocity approaches seismic rates, *Nature*, *427*, 436–439, doi:10.1038/nature02249.
- Drucker, D. C., and W. Prager (1952), Soil mechanics and plastic analysis of limit design, *Q. Appl. Math.*, *10*, 157–165.
- Dreger, D., and D. Helmberger (1991), Soil parameters of the Sierra Madre earthquake from regional and local body waves, *Geophys. Res. Lett.*, *18*(11), 2015–2018.
- Duan, B., and S. M. Day (2008), Inelastic strain distribution and seismic radiation from rupture of a fault kink, *J. Geophys. Res.*, *113*(B12), 1–19, doi:10.1029/2008JB005847.
- Dunham, E. M., D. Belanger, L. Cong, and J. E. Kozdon (2011a), Earthquake ruptures with strongly rate-weakening friction and off-fault plasticity. Part 1: Planar faults, *Bull. Seismol. Soc. Am.*, *101*, 2296–2307, doi:10.1785/0120100075.
- Dunham, E. M., D. Belanger, L. Cong, and J. E. Kozdon (2011b), Earthquake ruptures with strongly rate-weakening friction and off-fault plasticity. Part 2: Nonplanar faults, *Bull. Seismol. Soc. Am.*, *101*, 2308–2322, doi:10.1785/0120100076.
- Ely, G. P., S. M. Day, and J.-B. H. Minster (2008), A support-operator method for viscoelastic wave modeling in 3-D heterogeneous media, *Geophys. J. Int.*, *172*(1), 331–344, doi:10.1111/j.1365-246X.2007.03633.x.
- Ely, G. P., S. M. Day, and J.-B. H. Minster (2009), A support-operator method for 3-D rupture dynamics, *Geophys. J. Int.*, *177*(3), 1140–1150, doi:10.1111/j.1365-246X.2009.04117.x.
- Ely, G. P., S. M. Day, and J.-B. H. Minster (2010), Dynamic rupture models for the southern San Andreas Fault, *Bull. Seismol. Soc. Am.*, *100*(1), 131–150, doi:10.1785/0120090187.
- Goldsby, D. L., and T. E. Tullis (2011), Flash heating leads to low frictional strength of crustal rocks at earthquake slip rates, *Science*, *334*, 216–218, doi:10.1029/1126/science.1207902.
- Griffith, W. A., S. Nielsen, G. Di Toro, and S. A. F. Smith (2010), Rough faults, distributed weakening, and off-fault deformation, *J. Geophys. Res.*, *115*, B08409, doi:10.1029/2009JB006925.
- Han, R., T. Hirose, and T. Shimamoto (2010), Strong velocity weakening and powder lubrication of simulated carbonate faults at seismic slip rates, *J. Geophys. Res.*, *115*, B03412, doi:10.1029/2008JB006136.
- Hanks, T. C. (1982), f_{max} , *Bull. Seismol. Soc. Am.*, *72*(6), 1867–1879.
- Harris, R. A., et al. (2009), The SCEC/USGS dynamic earthquake rupture code verification exercise, *Seismol. Res. Lett.*, *80*(1), 119–126, doi:10.1785/gssrl.80.1.119.
- Hok, S., M. Campillo, F. Cotton, P. Favreau, and I. Ionescu (2010), Off-fault plasticity favors the arrest of dynamic ruptures on strength heterogeneity: Two-dimensional cases, *Geophys. Res. Lett.*, *37*(2), L02306, doi:10.1029/2009GL041888.
- Kame, N., and K. Uchida (2008), Seismic radiation from dynamic coalescence, and reconstruction of dynamic source parameters on a planar fault, *Geophys. J. Int.*, *174*(2), 696–706, doi:10.1111/j.1365-246X.2009.03849.x.

- Klinger, Y., R. Michel, and G. C. P. King (2006), Evidence for an earthquake barrier model from Mw~7.8 Kokoxili (Tibet) earthquake slip-distribution, *Earth Planet. Sci. Lett.*, 242, 354–364. doi:10.1016/j.epsl.2005.12.003.
- Lewis, M. A., and Y. Ben-Zion (2010), Diversity of fault zone damage and trapping structures in the Parkfield section of the San Andreas Fault from comprehensive analysis of near fault seismograms, *Geophys. J. Int.*, 183(3), 1579–1595, doi:10.1111/j.1365-246X.2010.04816.x
- Lin, P.-S., B. S.-J. Chiou, N. A. Abrahamson, M. Walling, C.-T. Lee, and C.-T. Cheng (2011), Repeatable source, site, and path effects on the standard deviation for empirical ground-motion prediction models, *Bull. Seismol. Soc. Am.*, 101(5), 2281–2295, doi:10.1785/0120090312.
- Ma, S., and D. J. Andrews (2010), Inelastic off-fault response and three-dimensional dynamics of earthquake rupture on a strike-slip fault, *J. Geophys. Res.*, 115(B4), 1–16. doi:10.1029/2009JB006382.
- Madariaga, R. (1977), High-frequency radiation from crack (stress drop) models of earthquake faulting, *Geophys. J. Roy. Astr. Soc.*, 51, 625–651.
- Marsaglia, G., and T. A. Bray (1964), A convenient method for generating normal variables, *SIAM Rev.*, 6(3), 260–264.
- Morikawa, N., T. Kanno, A. Narita, H. Fujiwara, T. Okumura, Y. Fukushima, and A. Guerpinar (2008), Strong motion uncertainty determined from observed records by dense network in Japan, *J. Seismol.*, 12(4), 529–546, doi:10.1007/s10950-008-9106-2.
- Noda, H., E. M. Dunham, and J. R. Rice (2009), Earthquake ruptures with thermal weakening and the operation of major faults at low overall stress levels, *J. Geophys. Res.*, 114(B7), 1–27. doi:10.1029/2008JB006143.
- Olsen, K. B., S. M. Day, J. B. Minster, Y. Cui, A. Chourasia, D. Okaya, P. Maechling, and T. H. Jordan (2008), TeraShake2: Spontaneous rupture simulations of Mw 7.7 earthquakes on the southern San Andreas Fault, *Bull. Seismol. Soc. Am.*, 98(3), 1162–1185, doi:10.1785/0120070148.
- Olsen, K. B., et al. (2009), ShakeOut-D: Ground motion estimates using an ensemble of large earthquakes on the southern San Andreas Fault with spontaneous rupture propagation, *Geophys. Res. Lett.*, 36(4), 1–6, doi:10.1029/2008GL036832.
- Palmer, A. C., and J. R. Rice (1973), The growth of slip surfaces in the progressive failure of over-consolidated clay, *Proc. R. Soc. London A*, 332, 527–548.
- Power, M., B. S.-J. Chiou, N. Abrahamson, Y. Bozorgnia, T. Shantz, and C. Roblee (2008), An overview of the NGA project, *Earthq. Spectra*, 24(1), 3–21, doi:10.1193/1.2894833.
- Power, W. L., and T. E. Tullis (1991), Euclidean and fractal models for the description of rock surface roughness, *J. Geophys. Res.*, 96, 415–424.
- Prakash, V. (1998), Frictional response of sliding interfaces subjected to time varying normal pressures, *J. Tribol.*, 120, 97–102.
- Prakash, V., and R. J. Clifton (1993), Time resolved dynamic friction measurements in pressure-shear, in *Experimental Techniques in the Dynamics of Deformable Solids*, edited by A. K. T. Ramesh, 33–48 pp., Appl. Mech. Div., Am. Soc. of Mechanical Eng., New York.
- Renard, F., C. Voisin, D. Marsan, and J. Schmittbuhl (2006), High resolution 3-D laser scanner measurements of a strike-slip fault quantify its morphological anisotropy at all scales, *Geophys. Res. Lett.*, 33, L04305, doi:10.1029/2005GL025038.
- Replogle, C. T. (2011), Corestone and saprock development in a zone of precariously balanced rocks, Peninsular Ranges, southern California: Speculations on the effects of ground shaking during earthquakes, M.S. thesis, San Diego State University, San Diego, CA.
- Rice, J. R. (1983), Constitutive relations for fault slip and earthquake instabilities, *Pure Appl. Geophys.*, 121(3), 443–475, doi:10.1007/BF02590151.
- Rice, J. R. (2006), Heating and weakening of faults during earthquake slip, *J. Geophys. Res.*, 111(B5), B05311, doi:10.1029/2005JB004006.
- Rockwell, T. K., and Y. Klinger (2013), Surface rupture and slip distribution of the 1940 Imperial Valley earthquake, Imperial Fault, Southern California: Implications for rupture segmentation and dynamics, *Bull. Seismol. Soc. Am.*, in press.
- Rockwell, T. K., S. Lindvall, T. Dawson, R. Langridge, W. Lttis, and Y. Klinger (2002), Lateral offsets on surveyed cultural features resulting from the 1999 Izmit and Duzce earthquakes, Turkey, *Bull. Seismol. Soc. Am.*, 92, 79–94.
- Rodriguez-Marek, A., G. A. Montalva, F. Cotton, and F. Bonilla (2011), Analysis of single-station standard deviation using the KiK-net data, *Bull. Seismol. Soc. Am.*, 101(3), 1242–1258, doi:10.1785/0120100252.
- Rojas, O., E. M. Dunham, S. M. Day, and L. A. Dalguer (2009), Finite difference modeling of rupture propagation with strong velocity-weakening friction, *Geophys. J. Int.*, 179, 1831–1858, doi:10.1111/j.1365-246X.2009.04387.x.
- Sagy, A., and E. E. Brodsky (2009), Geometric and rheological asperities in an exposed fault zone, *J. Geophys. Res.*, 114, B02301, doi:10.1029/2008JB005701.
- Sagy, A., E. E. Brodsky, and G. J. Axen (2007), Evolution of fault-surface roughness with slip, *Geology*, 35(3), 283–286, doi:10.1130/G23235A.1.
- Shashkov, M. (1996), *Conservative Finite-Difference Methods on General Grids*, CRC Press, Boca Raton, FL.
- Shi, Z., Y. Ben-Zion, and A. Needleman (2008), Properties of dynamic rupture and energy partition in a two-dimensional elastic solid with a frictional interface, *J. Mech. Phys. Solids*, 56, 5–24, doi:10.1016/j.jmps.2007.04.006.
- Shi, Z., A. Needleman, and Y. Ben-Zion (2010), Slip modes and partitioning of energy during dynamic frictional sliding between identical elastic-viscoplastic solids, *Int. J. Fract.*, 162, 51–67, doi:10.1007/s10704-009-9388-6.
- Simo, J. C., and T. J. R. Hughes (1998), *Computational Inelasticity*, Springer, New York.
- Templeton, E. L., and J. R. Rice (2008), Off-fault plasticity and earthquake rupture dynamics: I. Dry materials or neglect of fluid pressure changes, *J. Geophys. Res.*, 113, B09036, doi:10.1029/2007JB005529.
- Tsutsumi, A., and T. Shimamoto (1997), High-velocity frictional properties of gabbro, *Geophys. Res. Lett.*, 24(6), 699–702.
- Xu, S., Y. Ben-Zion, and J.-P. Ampuero (2012), Properties of inelastic yielding zones generated by in-plane dynamic ruptures: II. Detailed parameter-space study, *Geophys. J. Int.*, 191(3), 1343–1360, doi:10.1111/j.1365-246X.2012.05685.x.
- Zheng, G., and J. R. Rice (1998), Conditions under which velocity-weakening friction allows a self-healing versus a cracklike mode of rupture, *Bull. Seismol. Soc. Am.*, 88, 1466–1483.